

# Effects of Calcium on Strength and Microstructural Evolution of Extruded Alloys Based on Mg-3Al-1Zn-0.3Mn



Z.R. ZENG, Y.M. ZHU, J.F. NIE, S.W. XU, C.H.J. DAVIES, and N. BIRBILIS

A family of alloys based on the Mg-Al-Zn-Ca-Mn system (Mg-3Al-1Zn-1Ca-0.3Mn, Mg-3Al-1.5Zn-0.5Ca-0.3Mn, and Mg-3Al-1Ca-0.3Mn, wt pct) was developed for extrusion. Their mechanical properties were evaluated by tensile testing at room temperature, and compared to those of the benchmark Mg-alloy Mg-3Al-1Zn-0.3Mn (AZ31). The microstructures of the extruded alloys were characterized in detail in order to reveal the effect of Ca on microstructural evolution, and consequently the alloy strength. The addition of Ca to the AZ31 stifles dynamic recrystallization and grain growth, with only ~30 pct recrystallization and a recrystallized grain size of ~480 nm. In contrast, the benchmark alloy is essentially completely recrystallized with an average grain size of ~2.3  $\mu\text{m}$ . A high density of low-angle grain boundaries (LAGBs) and dislocations were observed in Ca-containing alloys, and were identified as a major factor in the observed strengthening. Such LAGBs form cellular subgrains predominantly along initial grain boundaries, or newly formed boundaries that are closely spaced (~600 nm) and nearly parallel to the extrusion direction. The subgrains have an ultrafine size of 100 to 400 nm, and difficult to convert to recrystallized grains. Solute segregation to grain boundaries was also observed. It is hypothesized that it is the Ca segregation to dislocation cores along LAGBs that decreases the dislocation mobility and stabilizes LAGBs, by thermodynamically decreasing the dislocation energy and/or kinetically imposing a solute drag effect.

<https://doi.org/10.1007/s11661-019-05318-6>

© The Minerals, Metals & Materials Society and ASM International 2019

## I. INTRODUCTION

MAGNESIUM (Mg) is the lightest structural metals and is now finding increased use in the transportation industry.<sup>[1-3]</sup> Currently, the most widely used Mg-alloys for engineering applications are cast alloys, and the adoption of Mg extrusion alloys has in contrast been quite limited.<sup>[4-6]</sup> Compared with aluminum extrusion alloys, the Mg extrusion alloys typically have lower extrudability, poorer corrosion resistance, and lower strength. Thus, improving the strength of Mg extrusion alloys would overcome a significant barrier for the wider

adoption of Mg extrusion alloys. In the last two decades, considerable efforts have been made to fabricate high-strength Mg extrusion alloys. Essentially, even without designing a new alloy, the commodity alloy Mg-3Al-1Zn-0.3Mn (AZ31) extrusion can be significantly strengthened by tailoring the grain size to the submicron scale, *via* low-temperature extrusion at 175 °C.<sup>[7]</sup> However, low-temperature extrusion leads to tool wear in an industrial context. If extrusion temperature is increased, then grain growth tends to increase significantly, leading to coarse-grained structures and low strength. Therefore, there still remain optimization possibilities for alloy composition to produce high-strength Mg extrusion alloys.

With respect to alloy design, the general approach adopted to date is to add a high concentration of rare-earth (RE) elements, such as Gd, Nd, Y, *etc.* For example, when produced by rapid solidification and hot extrusion, Mg-6.7Y-2.5Zn alloy has an exceptionally high strength of ~610 MPa, which is comparable to the high-strength Al-alloy AA7075-T6.<sup>[8]</sup> In addition, Mg-RE extrusions produced from bulk cast alloys can also have high strength. The strength of Mg-10Gd-5.7Y-1.6Zn-0.7Zr alloy is as high as 473 MPa.<sup>[9]</sup> Combined with other thermomechanical processing methods, such as rolling, the strength of

Z.R. ZENG, Y.M. ZHU, and J.F. NIE are with the Department of Materials Science and Engineering, Monash University, Clayton, VIC 3800, Australia. Contact e-mail: jianfeng.nie@monash.edu S.W. XU is with the Research Institute (R & D Center), Baoshan Iron & Steel Co., Ltd, Shanghai 201900, China. Contact e-mail: xushiwei@baosteel.com C.H.J. DAVIES is with the Department of Mechanical and Aerospace Engineering, Monash University, Clayton, VIC 3800, Australia. N. BIRBILIS is with the Department of Materials Science and Engineering, Monash University and also with the College of Engineering and Computer Science, Australian National University, Canberra, ACT 2601, Australia.

Manuscript submitted March 4, 2019.

Article published online June 17, 2019

Mg-RE-based alloys can be further increased.<sup>[10,11]</sup> The high strength in the Mg-RE-based alloy is caused by the combined effect of fine grains and effective hardening from different types nanoprecipitates.<sup>[9,12,13]</sup> Although the strength of Mg extrusions can be effectively improved by the major addition of rare-earth elements, such alloying addition will—rather significantly— increase the alloy cost and the alloy density.

Several RE-free high-strength Mg extrusion alloys have been reported to date, predominantly based on the Mg-Sn-Zn<sup>[14–16]</sup> and Mg-Ca alloy systems.<sup>[17,18]</sup> The yield strength of Mg-Sn based alloy is up to ~ 370 MPa, while the yield strength of Mg-Ca-based alloys can be as high as ~ 420 MPa. Recently, the Ca-containing magnesium wrought alloys have attracted significant research interests, as the Ca-containing alloys have demonstrated several advantageous mechanical properties. For those alloys with high Ca concentration, *e.g.*, > 2 wt pct, much beyond the solubility of Ca in Mg (~ 1 wt pct at 500 °C<sup>[19]</sup>), the high strength alloy can be fabricated *via* extrusion. For example, the Mg-3.5Al-3.3Ca-0.4Mn alloy has a yield strength of 410 MPa.<sup>[17]</sup> Given that Al and Ca are comparatively cheap and light-weight elements compared to RE and Sn, the low-cost Mg-Al-Ca-Mn-based alloys are anticipated candidates to replace expensive Mg-RE-based alloys for high-strength applications. Recent research in this field focuses on the alloys with dilute Ca addition, which is an effective replacement of RE, because the dilute Ca addition to Mg-(Al)-Zn-based alloy can also weaken basal texture,<sup>[20–23]</sup> improving ductility and formability,<sup>[24–27]</sup> alter deformation mechanism,<sup>[28,29]</sup> and increase extrudability.<sup>[30,31]</sup> However, the significant strengthening effect caused by microalloying of Ca has not yet been reported.

Having demonstrated that the high-strength Mg-Al-Ca-Mn alloys can be produced, the strengthening mechanism has not been systematically studied yet. For example, if Ca is added to the AZ31 alloy, how much strengthening can be induced by the Ca addition? In the previous report,<sup>[17]</sup> the strengthening mechanism is qualitatively attributed to the combined effect of dynamically recrystallized fine grains, nanoscale precipitate, and a strong basal texture. What is the major factor for the high strength of an Mg-Al-Ca-Mn alloy? If the Ca concentration is decreased to dilute level, will the high strength in the Mg-Al-Ca-Mn alloy be retained? In order to clarify the effect of Ca on alloy strengthening, Mg-3Al-1Zn-1Ca-0.3Mn, Mg-3Al-1.5Zn-0.5Ca-0.3Mn, and Mg-3Al-1Ca-0.3Mn alloys are prepared in this study. AZ31 alloy is the benchmark alloy. After extrusion under the same condition, the alloy strengths are measured, and their microstructures are characterized to establish the composition–microstructure–property relationship. Using the advanced characterization techniques such as high-resolution transmission Kikuchi diffraction (TKD), the effects of Ca addition on the microstructural evolution during the extrusion process is clearly illustrated, allowing the origin of the Ca-alloying-induced strengthening to be discussed.

## II. EXPERIMENTAL PROCEDURES

Magnesium alloys Mg-3Al-1Zn-0.3Mn, Mg-3Al-1Zn-0.5Ca-0.3Mn, Mg-3Al-1Zn-1Ca-0.3Mn, and Mg-3Al-1Ca-0.3Mn were cast at 760 °C under argon atmosphere protection. The as-cast ingots were homogenized at 400 °C for 24 hours, and then quenched in cold water. The as-homogenized ingots were extruded from 35 mm to 8 mm in diameter at 210 °C and 250 °C with a ram speed of 0.1 mm/s, and at 300 °C with a ram speed of 0.8 mm/s. The as-extruded bars were machined to tensile test samples with a gauge length of 10 mm. The tension tests were performed at the Instron 4505 machine at room temperature, with the crosshead displacement speed of 0.6 mm/min, corresponding to the initial strain rate of 10<sup>-3</sup>/s. Three specimens were tested for each condition.

The samples for X-ray diffraction (XRD) and electron backscattered diffraction (EBSD) were polished using silicon carbide paper and 50-nm-diameter silica suspension. The samples for TKD and scanning transmission electron microscopy (STEM) were 3-mm-diameter disks, prepared by mechanical grinding to 0.05 mm and ion polishing using Gatan precision ion-polishing system at 4.8 kV and 4 °C and – 60 °C until a hole is formed in the sample.

Diffraction profiles of (10 $\bar{1}$ 0), (0002), and (10 $\bar{1}$ 1) peaks were measured using a Bruker D8 Advance X-ray diffractometer using Cu-K $\alpha$  radiation ( $\lambda = 0.154$  nm) operating at 40 kV and 40 mA. Sample dislocation density was calculated from the half-width of the diffraction peaks using TOPAS 4.2 software. Sample texture was measured using GBC-MMA diffractometer using Cu-K $\alpha$  radiation operating at 40 kV and 25 mA. The (0002), (10 $\bar{1}$ 0), (10 $\bar{1}$ 1), and (10 $\bar{1}$ 2) pole figures were collected on a 5 deg grid up to 75 deg sample tilt. Data were analyzed using the Textool software to generate orientation distributions and recalculate pole figures.

EBSD and TKD were performed using a FEI 3D Quanta FEG scanning electron microscope equipped with a Pegasus Hikari detector and with a TSL-OIM control system. EBSD technique was used to characterize the AZ31 samples extruded at 250 °C and 300 °C, which were fully recrystallized with a grain size above 1  $\mu$ m. For the partially recrystallized samples (Ca-containing alloys), or for the recrystallized sample but with the grain size smaller than 1  $\mu$ m (AZ31 extruded at 210 °C), TKD technique was used. For TKD, rather than using the bulk sample, the electron transparent sample, *e.g.*, thin foil for TEM, was used, and the diffraction source volume is consequently reduced significantly. Compared with conventional EBSD, TKD provides much higher spatial resolution, with the resolution of down to 2 nm.<sup>[32]</sup> Moreover, TKD will provide much-improved indexing rate for the heavily deformed sample, which is always a problem faced while using conventional EBSD. This is because the high dislocation density and lattice distortion in the deformed sample will interact with an incident electron beam, leading to the blurred or missing Kikuchi pattern.<sup>[33]</sup> Consequently, a heavily deformed sample or area, such

as shear bands, which cannot be characterized by EBSD, can be clearly observed using TKD method. Therefore, TKD method is especially a suitable characterization method for the current study, as a high resolution and indexing rate are required to characterize the deformed microstructure and the early-stage configuration of recrystallized grains which have ultrafine size.

The step sizes used for EBSD and TKD were 250 nm and 15 nm, respectively. The EBSD and TKD data were processed using software TSL OIM 7. The high-angle grain boundary (HAGB) is defined as the boundary with misorientation  $> 15$  deg,<sup>[34]</sup> while the low-angle grain boundary (LAGB) is the boundary with misorientation between 2 and 15 deg. Grain is defined as the cellular structure enclosed by HAGB, and subgrain is the cellular structure enclosed by LAGB. The size of a grain is represented by the equivalent diameter that was calculated from the measured grain area by equation  $2\sqrt{\frac{\text{Grainarea}}{\pi}}$ . The average grain size under each condition was calculated by analyzing all grains in a single EBSD or TKD scan.

In-grain misorientation axis analysis is used to qualitatively estimate the geometrically necessary dislocation (GNDs) of different types in the extruded samples. GNDs are the dislocations that are statistically stored in materials, and contribute to the lattice orientation gradient.<sup>[35]</sup> By measuring misorientation between neighboring pixels in EBSD scanning, the misorientation axis (Taylor axis)—the crystallographic axis that crystal lattice under the action of GND bending around—can be calculated. The distribution of Taylor axis can provide qualitative information about the relative content of GNDs in different types. This method is known as in-grain misorientation axis analysis (IGMA), and has been introduced to analyze GNDs in Mg alloy by Miller *et al.*,<sup>[28]</sup> Chun *et al.*,<sup>[36]</sup> and Hadorn *et al.*<sup>[37]</sup> In brief, the Taylor axis [0001] corresponds to prismatic  $\{10\bar{1}0\}$   $\langle 1\bar{2}10 \rangle$  dislocation slip, while basal (0001)  $\langle 1\bar{2}10 \rangle$  and pyramidal II  $\{11\bar{2}2\}$   $\langle \bar{1}\bar{1}23 \rangle$  dislocation slips have the same Taylor axis  $\langle 1\bar{1}00 \rangle$ . IGMA analysis was performed in HKL Channel 5 software package as per the following procedures: (1) selecting a deformed grain, (2) exporting orientation information of the highlighted grain to an ‘ang’ format file, (3) importing to HKL Mambo and plotting misorientation axes for all possible neighboring measurement-point pairs in a standard unit triangle, and (4) contouring the density of the misorientation axes with the unit of mud (multiples of the uniform distribution). The minimum and maximum misorientation angles included in the analysis are set at 0.5 and 5 deg, respectively.

The atomic-resolution high-angle annular dark field (HAADF)-STEM images were obtained using a double-corrected FEI Titan 80 to 300 transmission electron microscope operating at 300 kV. A 15-mrad convergence semi-angle was used, corresponding to 0.12 nm resolution. Energy-dispersive X-ray spectroscopy (EDXS) maps

were obtained in STEM mode using a FEI F20 transmission electron microscope equipped with a Bruker XFlash 6TI30 EDX detector.

### III. RESULTS

#### A. Mechanical Property and Microstructure of Mg-Al-Zn-Ca-Mn and AZ31 Extrusion Alloys

Figures 1(a) through (c) show the engineering stress–strain curves of AZ31 and Mg-3Al-1Zn-1Ca-0.3Mn alloys extruded at different temperatures. After extrusion at 210 °C, AZ31 and Mg-3Al-1Zn-1Ca-0.3Mn alloys had a yield strength of 355 MPa and 414 MPa, respectively. However, the total elongation of the Mg-3Al-1Zn-1Ca-0.3Mn alloy was very low—only  $\sim 2.5$  pct. When the extrusion temperature was increased to 250 °C, the yield strength of Mg-3Al-1Zn-1Ca-0.3Mn alloy was almost unchanged, but the total elongation was enhanced to  $\sim 7$  pct. In contrast, the yield strength of AZ31 was decreased from 355 MPa to 317 MPa, after the extrusion temperature was increased from 210 °C to 250 °C. The further increase in extrusion temperature to 300 °C led to the decreased yield strength: 330 MPa for Mg-3Al-1Zn-1Ca-0.3Mn and 242 MPa for AZ31. The mechanical properties of AZ31 and Mg-3Al-1Zn-1Ca-0.3Mn alloys extruded at different temperatures are summarized in Table I. It can be seen that the Ca addition led to the most significant strengthening effect when the alloy was extruded at 250 °C.

In order to optimize the tensile property, the extrusion temperature and speed were kept at 250 °C and 0.1 mm/s, but the alloy composition was modified to Mg-3Al-1.5Zn-0.5Ca-0.3Mn and Mg-3Al-1Ca-0.3Mn. When the Zn:Ca ratio was changed from 1:1 to 1.5:0.5, the yield strength of resultant Mg-3Al-1.5Zn-0.5Ca-0.3Mn dropped to 380 MPa, Figure 1(d). In another case, when the Ca concentration was kept at 1 wt pct, but Zn was removed from the Mg-3Al-1Zn-1Ca-0.3Mn alloy, the yield strength of the resultant Mg-3Al-1Ca-0.3Mn alloy was only dropped slightly from 413 MPa to 408 MPa. After the extrusion temperature increased to 300 °C, both Mg-3Al-1.5Zn-0.5Ca-0.3Mn and Mg-3Al-1Ca-0.3Mn alloys had decreased strengths, about 323 MPa and 338 MPa, respectively.

Two points can be drawn from the tensile tests. (i) Ca is more important for strengthening than Zn in the Mg-Al-Zn-Ca-Mn alloys. Whilst the addition of 1 wt pct Ca to Mg-Al-Zn-Mn alloy resulted in a greater strengthening effect of 88 to 96 MPa, the addition to 1 wt pct Zn to Mg-Al-Ca-Mn alloy only led to a marginal increment in strength. (ii) Mg-Al-Zn-Ca-Mn based alloy can achieve high strength over 400 MPa and reasonable ductility after they are extruded at 250 °C. Therefore, alloys extruded at 250 °C are examined in detail in the following sections.

Figures 2(a) through (d) show the microstructures of AZ31, Mg-3Al-1Zn-1Ca-0.3Mn, Mg-3Al-1.5Zn-0.5-



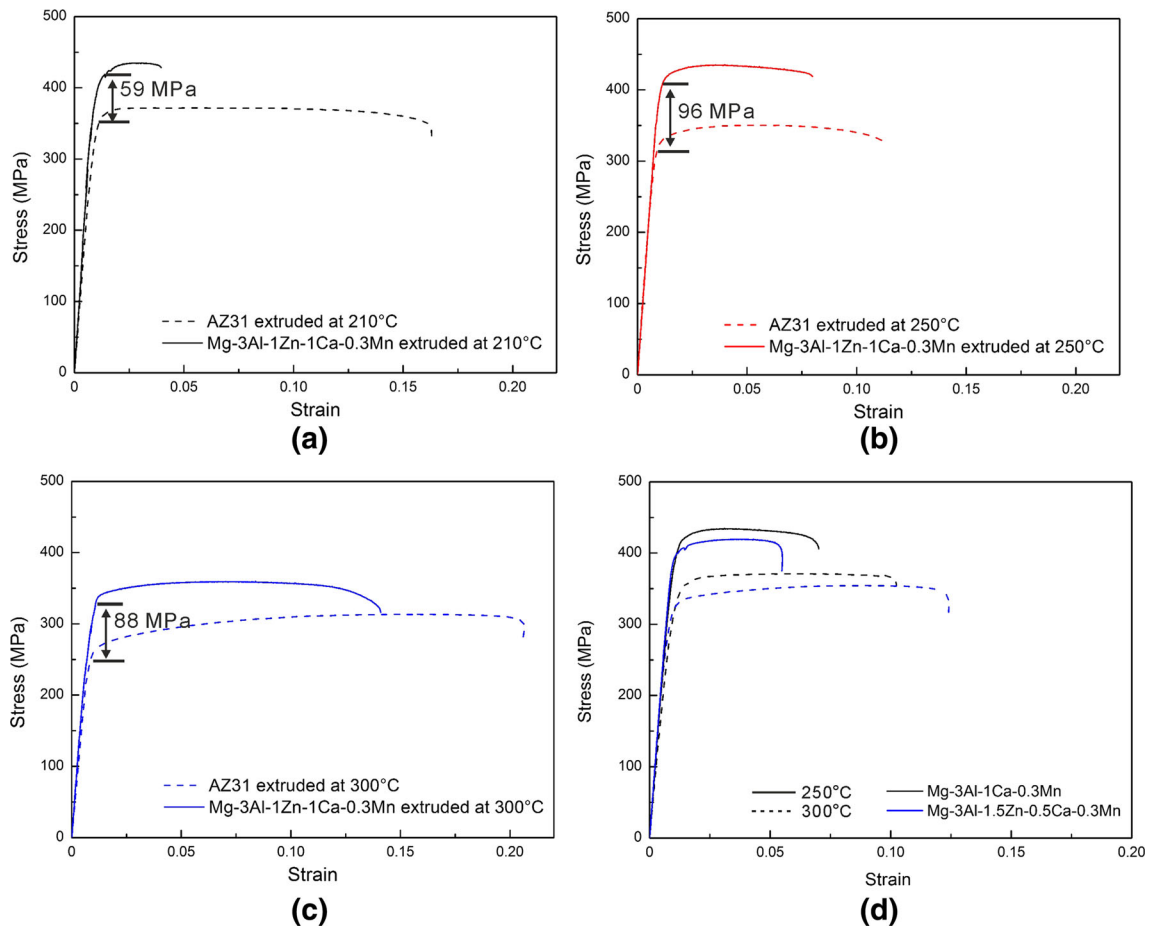


Fig. 1—Tensile stress–strain curves of AZ31 and Mg-3Al-1Zn-1Ca-0.3Mn alloys extruded at (a) 210 °C, (b) 250 °C, and (c) 300 °C in the tensile test at room temperature, and (d) Mg-3Al-1.5Zn-0.5Ca-0.3Mn and Mg-3Al-1Ca-0.3Mn alloys extruded at 250 °C and 300 °C.

Ca-0.3Mn, and Mg-3Al-1Ca-0.3Mn alloys extruded at 250 °C. The AZ31 was recrystallized with fully equiaxed grains. The averaged grain sizes of AZ31 was 2.3  $\mu\text{m}$  (Figures 2(a) and (e)). In contrast, the Mg-3Al-1Zn-1Ca-0.3Mn alloy was partially recrystallized with large deformed grains and small recrystallized grains. For the Mg-3Al-1Zn-1Ca-0.3Mn alloy, the area fraction of recrystallized grain was 30 pct and the averaged size of recrystallized grains was 0.48  $\mu\text{m}$  (Figures 2(b) and (f)). When the deformed grains and subgrains were taken into account, the average grain size of Mg-3Al-1Zn-1Ca-0.3Mn alloy was about 1.6  $\mu\text{m}$ , and HAGBs took about 42 pct of the grain boundaries.

Compared with Mg-3Al-1Zn-1Ca-0.3Mn alloy, the Mg-3Al-1.5Zn-0.5Ca-0.3Mn alloy had a larger area fraction of recrystallized grains (55 pct), a larger recrystallized grain size (0.71  $\mu\text{m}$  in average), and a higher fraction of HAGBs (48.9 pct), Figure 2(c). With respect to the Mg-3Al-1Ca-0.3Mn alloy, it had a microstructure similar to that of Mg-3Al-1Zn-1Ca-0.3Mn alloy despite the absence of Zn (Figure 2(d)), and the size and fraction of recrystallized grains were  $\sim$  0.48  $\mu\text{m}$  and  $\sim$  30 pct, respectively. The HAGBs were  $\sim$  38.5 pct of grain boundaries. The averaged grain sizes including the deformed grains and subgrains were measured to be 2.6  $\mu\text{m}$  and 2.1  $\mu\text{m}$  for the Mg-3Al-1.5Zn-0.5Ca-0.3Mn (Figure 2(g)) and

Mg-3Al-1Ca-0.3Mn alloys (Figure 2(h)). These microstructural features are listed in Table II.

Macrotecture of alloys were measured using X-ray diffraction (Figure 3(a) through (d)). The results suggested that the AZ31 benchmark and Ca-containing alloys had  $\langle 10\bar{1}0 \rangle // \text{ED}$  fiber texture, *i.e.*, the  $\langle 10\bar{1}0 \rangle$  axis was nearly parallel to the extrusion direction. However, the intensity of  $\langle 10\bar{1}0 \rangle // \text{ED}$  texture was different for each alloy. After extrusion at 250 °C, the AZ31 alloy had the weakest  $\langle 10\bar{1}0 \rangle // \text{ED}$  texture of 5.6 mrd. With the 1 wt pct addition of Ca, the Mg-3Al-1Zn-Ca-0.3Mn alloy had an increased texture intensity to 7.3 mrd. The higher texture intensity in the Mg-3Al-1Zn-1Ca-0.3Mn alloy was caused by the preservation of the deformed grains that were not recrystallized during the extrusion process. These deformed grains had strong  $\langle 10\bar{1}0 \rangle // \text{ED}$  texture. When the Zn and Ca concentrations were changed to 1.5 and 0.5 pct, respectively, the texture intensity of Mg-3Al-1.5Zn-0.5Ca-0.3Mn alloy was increased to 8.8 mrd. An even higher intensity of  $\langle 10\bar{1}0 \rangle // \text{ED}$  texture, about 10.8 mrd, was observed after Zn was removed from the Mg-3Al-1Zn-1Ca-0.3Mn alloy. Therefore, the combined additions of Zn and Ca in 1 wt pct in the Mg-3Al-1Zn-1Ca-0.3Mn alloy gave rise to the weakest texture.

**Table I. Tensile Properties of Alloys Extruded at 250 °C and 300 °C**

Alloy	Extrusion Temperature °C	TYS (MPa)	UTS (MPa)	Tensile Strain
Mg-3Al-1Zn-0.3Mn	250	317 ± 7	350 ± 2	0.142 ± 0.006
	300	242 ± 2	313 ± 6	0.198 ± 0.011
Mg-3Al-1Zn-0.5Ca-0.3Mn	250	380 ± 6	420 ± 3	0.051 ± 0.003
	300	330 ± 3	360 ± 4	0.135 ± 0.01
Mg-3Al-1Zn-1Ca-0.3Mn	250	413 ± 4	432 ± 5	0.075 ± 0.008
	300	323 ± 6	356 ± 3	0.118 ± 0.005
Mg-3Al-1Ca-0.3Mn	250	408 ± 2	432 ± 7	0.065 ± 0.009
	300	338 ± 9	372 ± 2	0.096 ± 0.006

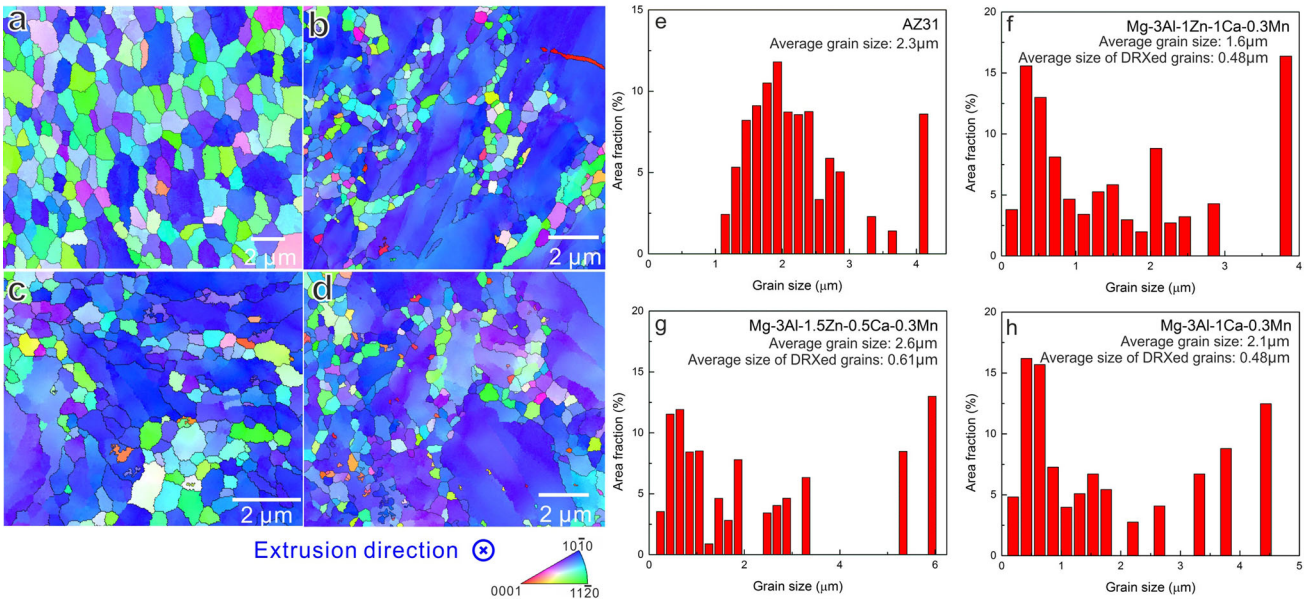


Fig. 2—TKD-orientation maps of (a) AZ31 (b) Mg-3Al-1Zn-1Ca-0.3Mn (c) Mg-3Al-1.5Zn-0.5Ca-0.3Mn and (d) Mg-3Al-1Ca-0.3Mn alloys extruded at 250 °C. (e through h) Histograms showing grain size distribution (including subgrains) of the alloys.

**Table II. Microstructural Characteristics of Alloy Extruded at 250 °C**

Alloy	Grain Size Including Subgrains (μm)	Area Fraction of DRXed Grains	Size of DRXed Grains (μm)	$\langle 10\bar{1}0 \rangle$ Texture Intensity (mrd)	Taylor Factor	Dislocation Density ( $\times 10^{14}/m^2$ )	HAGB Fraction	$\theta_{LAGB}$ (deg)
Mg-3Al-1Zn-0.3Mn	2.3	1	2.3	5.6	2.5	3.35	0.69	4.0
Mg-3Al-1.5Zn-0.5Ca-0.3Mn	2.6	0.44	0.61	8.8	3.7	5.68	0.48	4.2
Mg-3Al-1Zn-1Ca-0.3Mn	1.6	0.30	0.48	7.3	3.3	7.20	0.42	4.8
Mg-3Al-1Ca-0.3Mn	2.1	0.29	0.48	10.8	4.2	4.13	0.39	4.4

Figures 3(e) through (g) show the XRD  $\theta$ - $2\theta$  scanning profile of diffraction of  $(10\bar{1}0)$ ,  $(0002)$ , and  $(10\bar{1}1)$  crystal planes, respectively. The diffraction profiles were analyzed by assuming that the peak broadening is related to grain refinement and microstrain induced by dislocations.<sup>[38]</sup> By fitting the scanning profiles of  $(10\bar{1}0)$ ,  $(0002)$ , and  $(10\bar{1}1)$  peaks using the Double-Voigt approach,<sup>[39]</sup> the peak broadening induced by individual dislocations and grain refinement can be differentiated. The microstrains caused by dislocations in the AZ31

benchmark, Mg-3Al-1Zn-1Ca-0.3Mn, Mg-3Al-1.5Zn-0.5Ca-0.3Mn, and Mg-3Al-1Ca-0.3Mn alloys were estimated to be  $7.3 \times 10^{-4}$ ,  $1.1 \times 10^{-3}$ ,  $0.9 \times 10^{-4}$ , and  $0.8 \times 10^{-4}$ , respectively. Dislocation density ( $\rho$ ) was subsequently estimated from the microstrain ( $\epsilon$ ) according to the following equation<sup>[40,41]</sup>:

$$\rho \cong \frac{4\pi\epsilon^2}{Cb^2}, \quad [1]$$

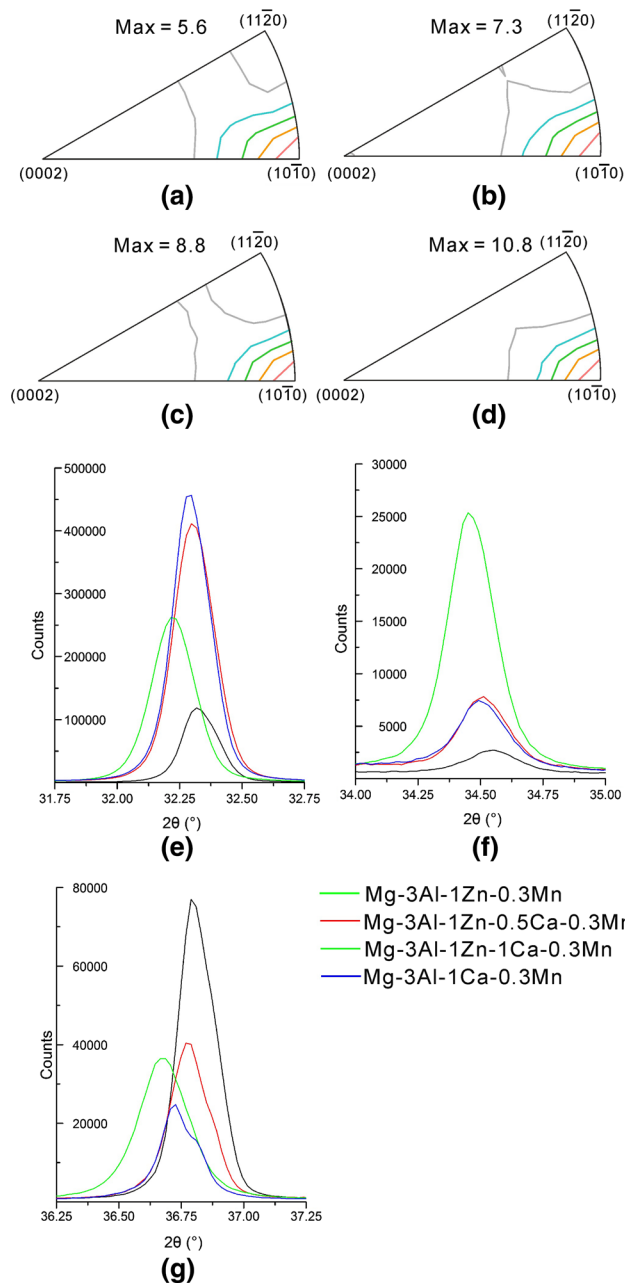


Fig. 3—XRD inverse pole figures along extrusion direction of (a) AZ31, (b) Mg-3Al-1Zn-1Ca-0.3Mn, (c) Mg-3Al-1.5Zn-0.5Ca-0.3Mn, and (d) Mg-3Al-1Ca-0.3Mn alloys extruded at 250 °C. XRD  $\theta$ -2 $\theta$  scan showing the diffraction peaks of (e) (10 $\bar{1}$ 0), (f) (0002), and (g) (1011) crystal planes of samples extruded at 250 °C.

where C is a constant that was determined as 0.19483 for Mg by Dragomir's work,<sup>[41]</sup> and  $b$  is the Burger's vector ( $3.2 \times 10^{-10}$  m for Mg). The measured dislocation densities are shown in Table II.

### B. Effect of Ca Addition on Microstructural Evolution During Extrusion

In order to reveal how Ca addition affected the microstructure of extruded alloys, the AZ31 benchmark and the Mg-3Al-1Zn-1Ca-0.3Mn alloy extruded at

250 °C were selected as the representatives. The sample microstructures at different positions in the extrusion die were examined, which demonstrated the microstructural evolution during extrusion (Figure 4). At the location before the die entrance, the Mg-3Al-1Zn-1Ca-0.3Mn alloy exhibited the typical as-deformed microstructure (Figure 4(a)). Lenticular twins were observed in deformed grains with intragranular orientation gradient. These twins had 86 deg  $\langle 11\bar{2}0 \rangle$  relationship to the surrounding matrix, and therefore they were extension twins (ETs). In the same location of the AZ31 alloy, a banana-shaped band was observed within the deformed matrix (Figure 4(b)). The band was composed of large elongated grains and many small equiaxed grains. The examination of grain orientation demonstrated that the elongated grains had a nearly 56 deg  $\langle 11\bar{2}0 \rangle$  orientation relationship to the surrounding deformed matrix, and therefore, they were contraction twins (CTs). Dynamic recrystallization (DRX) was also observed in the band.

In the half-way position where the cross section of extrusion was reduced from 35 to about 15 mm, both AZ31 benchmark and Mg-3Al-1Zn-1Ca-0.3Mn alloy were partially recrystallized. In the Mg-3Al-1Zn-1Ca-0.3Mn alloy, the recrystallized grains were observed, but they only occupied a minor area fraction, ~20 pct (Figure 4(c)). The averaged grain size was about 0.50  $\mu\text{m}$  in diameter. There were numerous boundaries nearly parallel to the extrusion direction within the deformed grains. The recrystallized grains were observed along these boundaries. At the same position of the AZ31 alloy, the area fraction of recrystallized grain was ~70 pct, and the deformed grains were surrounded by recrystallized grains (Figure 4(d)). The average size of recrystallized grains was 1.4  $\mu\text{m}$  in diameter.

At the exit of the die, Mg-3Al-1Zn-1Ca-0.3Mn alloy was still partially recrystallized. The deformed parent grains can still be recognized. For example, there were two deformed grains shown in Figure 4(e), colored green and red, respectively, in the orientation map. The area fraction of recrystallized grains was increased to about 30 pct. The average size of recrystallized grains was similar to those shown in Figure 5(d), about 0.52  $\mu\text{m}$  in diameter. In contrast, the AZ31 alloy was fully recrystallized (Figure 4(f)). The averaged grain size was increased to 1.8  $\mu\text{m}$  in diameter.

#### 1. Microstructural evolution in AZ31

The area highlighted by the dark rectangles in Figure 4(b) was closely examined to elucidate the early stage of recrystallization in the AZ31 alloy. This area was comparatively simple, containing only few recrystallized grains. It was observed that recrystallized grains, labeled 1 and 2, originated from a CT (Figures 5(a) through (b)). Grains 1 and 2 had similar orientations to the CT, but the dark contrast in image-quality map (Figure 5(c)) showed that they had well-defined LAGBs.<sup>[42]</sup> These grains had a small size, only about 0.5  $\mu\text{m}$  in diameter. The misorientation histogram along the yellow dashed line showed that boundary angle between Grain 1 and Grain 2 was ~2 deg, while that of Grain 2 and CT was ~5 deg (Figure 5(d)). Grains 1 and



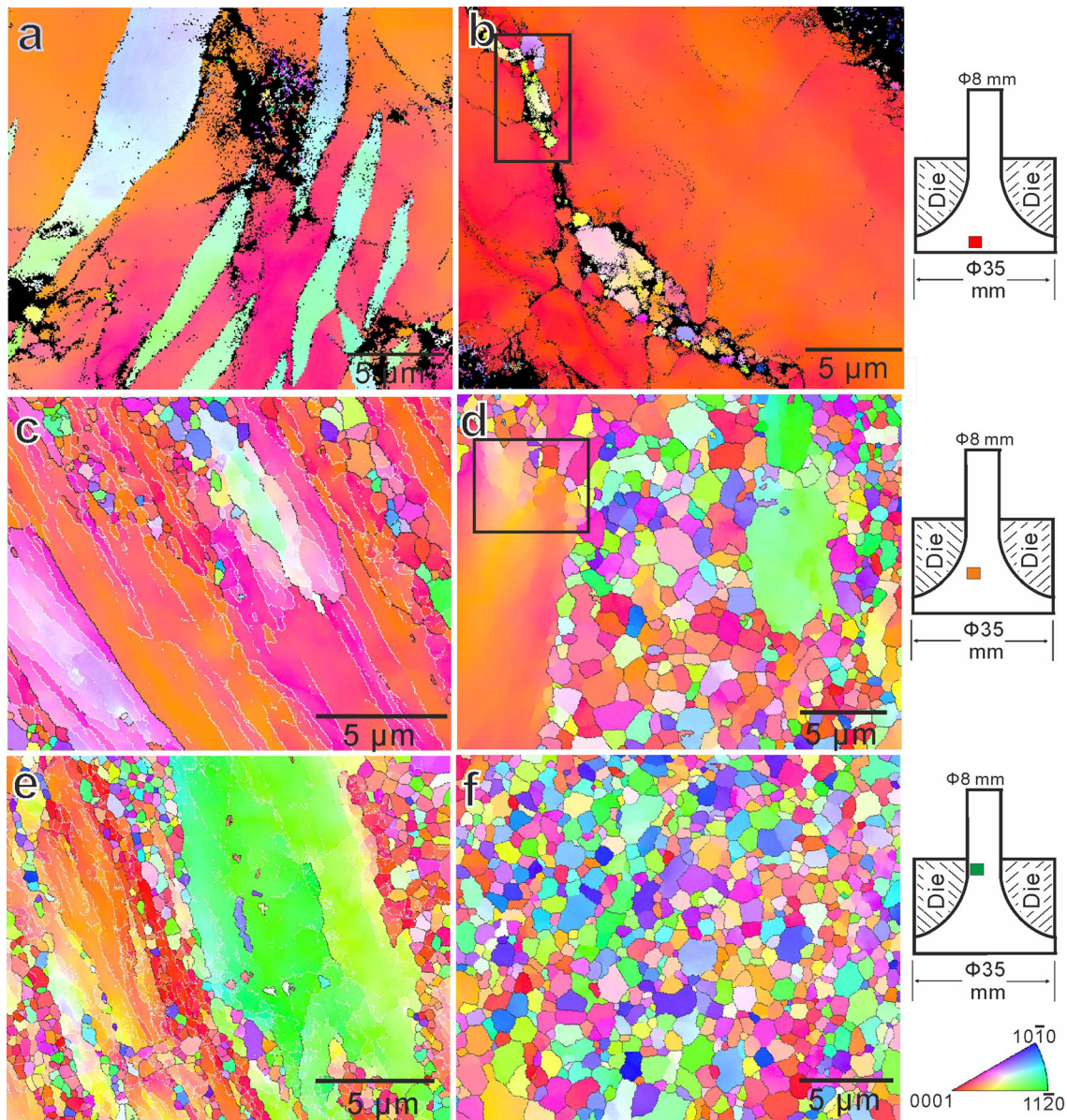


Fig. 4—TKD orientation maps showing sample microstructures at (a, b) entrance of die, (c, d) half-way in die, and (e, f) exit of die for (a, c, e) Mg-3Al-1Zn-1Ca-0.3Mn and (b, d, f) AZ31. Grain boundaries in dark and white indicating HAGBs and LAGBs, respectively.

2 were formed *via* subdivision of contraction twins by the formation of LAGBs. This DRX process is known as the twin-induced DRX, which was previously reported for Mg alloys.<sup>[43]</sup>

Compared to the recrystallized grains formed within twins, more grains were formed in the matrix near twin boundaries. These grains, numbered 3 to 7, were difficult to be identified in the orientation map (Figure 5(a)), because they had similar orientations to the matrix. However, as highlighted by the blue arrows in the image-quality map (Figure 5(c)), well-defined LAGBs were observed as a signature of DRX. The orientation relationships of grains 3 to 7 to the matrix were 5.1 deg  $[3\bar{1}214]$ , 7.7 deg  $[21\bar{3}18]$ , 6.1 deg  $[2\bar{1}\bar{1}20]$ , 3.4 deg  $[2\bar{1}\bar{1}26]$ , and 3.1 deg  $[10\bar{1}18]$ , respectively. The misorientation

axis was almost close to the  $[0001]$  axis. The size of these grains ranged from 0.4 to 1  $\mu\text{m}$  in diameter.

With the progress of extrusion, the deformation twins in the AZ31 alloy were not observed. In the grains highlighted by the dark rectangle in Figure 4(d), numerous subgrains were observed along the grain boundaries (Figure 6(a) through (c)). These subgrains had similar orientations to their deformed parent grain. A large orientation gradient was observed from the boundary to the center of the deformed grain, and the orientation was measured to vary nearly linearly along the dark line in Figure 6(d). Once the subgrains were formed, the total orientation gradient did not change, but the orientation gradient within the subgrains was greatly reduced (the blue line in Figure 6(d)). In another

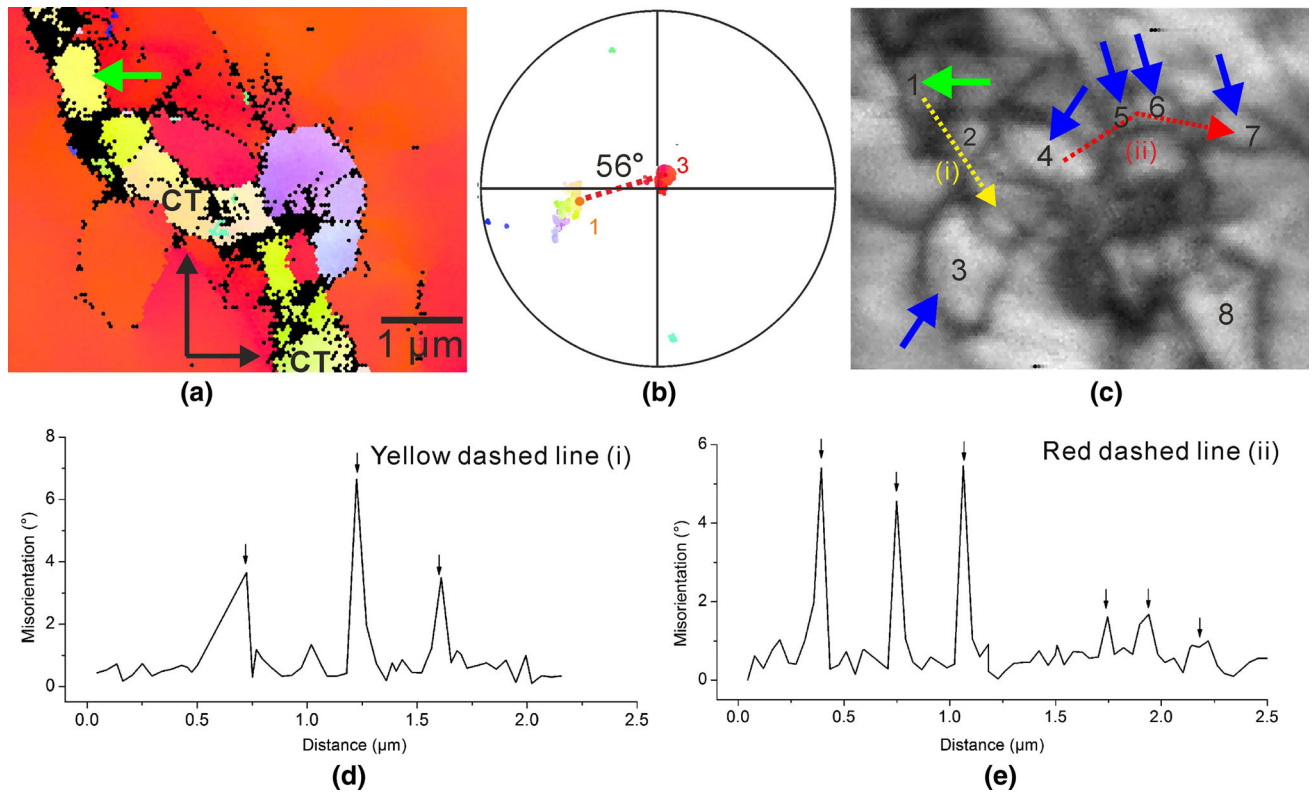


Fig. 5—(a) TKD orientation map, (b) pole figure, and (c) image-quality map showing deformation twins and dynamically recrystallized grains within twin bands in Mg-3Al-1Zn-0.3Mn (AZ31) alloy. Histograms showing point-to-point misorientation along (d) yellow and (e) red line profiles in the image-quality map.

deformed grain of the AZ31 alloy (Figures 6(e) and (f)), LAGBs highlighted by the arrows in Figure 6(f) were observed to subdivide the deformed grains into several smaller ones with similar orientation to each other. The smaller grains had an irregular shape and the significant orientation gradient; therefore, such grains were still deformed grains.

## 2. Microstructural evolution in the Mg-3Al-1Zn-1Ca-0.3Mn alloy

The DRX behavior of the Mg-3Al-1Zn-1Ca-0.3Mn alloy was examined. Figure 7(a) shows an ET, which was intersected by a CT. The ET and CT had 86 deg  $\langle 11\bar{2}0 \rangle$  and 56 deg  $\langle 11\bar{2}0 \rangle$  orientation relationship to the matrix, respectively (Figure 7(b)). In the band that was composed of two contract twins and matrix between them (highlighted by the green dashed lines in Figure 7(c)), dense LAGBs were observed, and they subdivided the band into fine and dense cellular subgrains. The average size of the cellular grains was ultrafine, about 0.1 to 0.3  $\mu\text{m}$  in diameter. In addition to the twin band, there were microbands with a high density of LAGBs nearly along the extrusion direction (highlighted by the red dashed lines in Figure 7(c)).

With the progress of the extrusion process, the microbands in the Mg-3Al-1Zn-1Ca-0.3Mn alloy could be observed more clearly in the deformed grains. Figure 8a shows three microbands, numbered 1, 2, and 3, which contained one or two layers of fine

recrystallized grains. Among these bands, bands 2 and 3 were parallel and along the extrusion direction, while band 1 (highlighted by the dark rectangle) intersected the band 2 (highlighted by the orange rectangle). A closer examination showed that the grains in the microbands 2 and 3 did not have any twin orientation relationship with the matrix or to each other. In contrast, the microband 1 was essentially composed of deformation twins, including CT, contraction–contraction double twins (DT), and contraction–extension double twins (CT-ET), Figure 8(b). The image-quality map (Figure 8(c)) showed that LAGBs were formed in the CT, DT and CT-ET double twin, and then subdivided the twins to a cellular subgrains, which represented the early-stage configuration of recrystallized grains. Although some subgrains formed in the twins, the number of these subgrains was much less than the number of recrystallized grains in the microbands 2 and 3. Therefore, the twin-induced nucleation was identified as a minor mechanism of DRX in the Mg-3Al-1Zn-1Ca-0.3Mn alloy.

Having established that recrystallization behavior in microbands 2 and 3 is more important, how the recrystallized grains formed in these microbands needs to be further investigated. In order to reveal the origin of DRX in microbands, the grain boundaries right next to the microband 3 were examined. These boundaries were highlighted by a red rectangle in Figure 8(a) and numbered microband 4. In microband 4, two long and



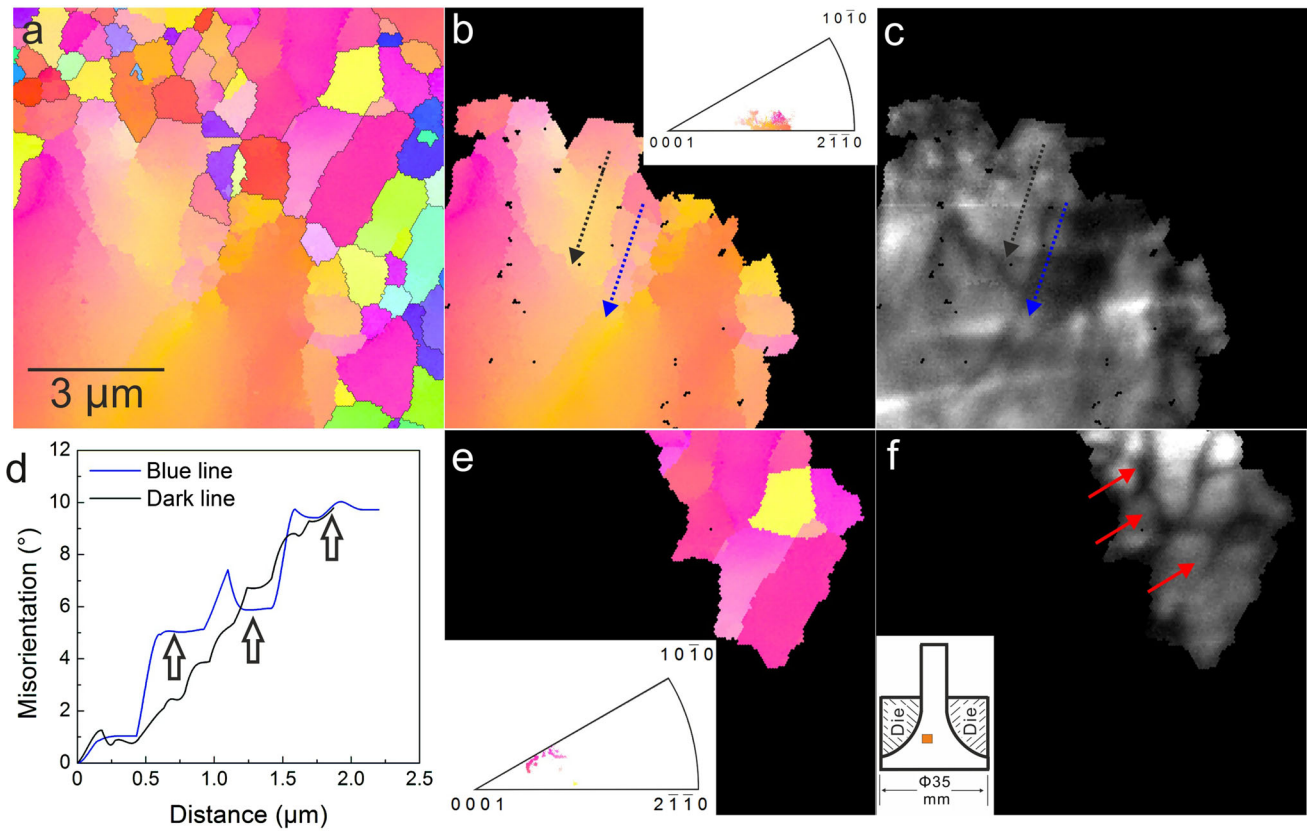


Fig. 6—(a) TKD orientation map of a partially recrystallized AZ31 alloy, and (b, e) TKD orientation and (c, f) image-quality map of two deformed grains. (d) Histograms showing point-to-origin misorientation along line profiles in (c).

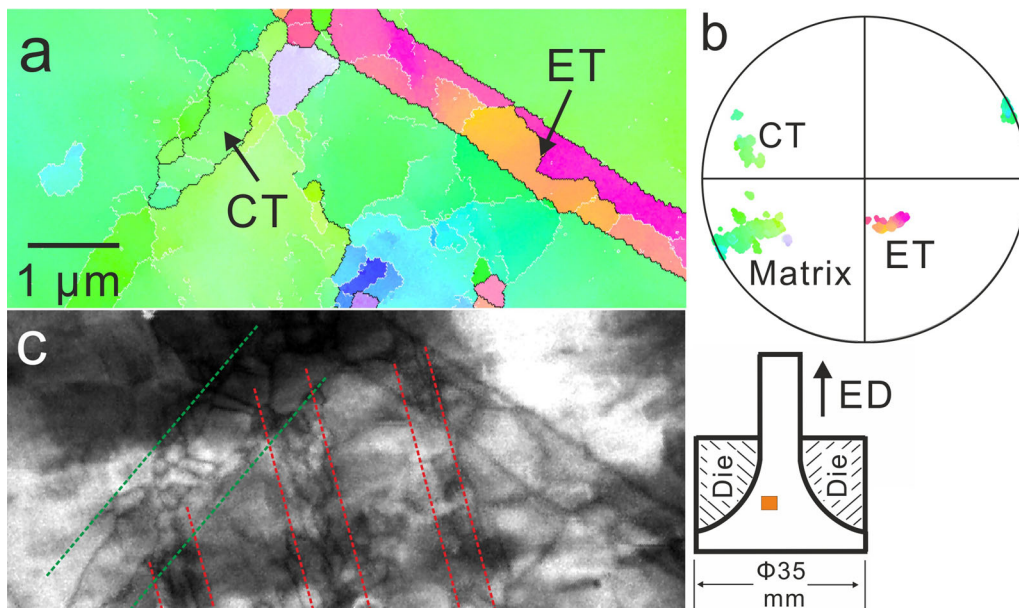


Fig. 7—(a) TKD orientation map, (b) (0002) pole figure, and (c) image-quality map of a partially recrystallized Mg-3Al-1Zn-1Ca-0.3Mn alloy. Grain boundaries in dark and white color indicating HAGBs and LAGBs, respectively.

straight boundaries were observed parallel to the extrusion direction. The interboundary space was  $\sim 600$  nm (Figure 9(a)). The left boundary had an average misorientation of about 18 deg. The right boundary was still a

LAGB, whose average misorientation was 8.3 deg. The superimposition of orientation map and image-quality map (Figure 9(b)) showed a string of subgrains, which had a straight linear-chain configuration along the

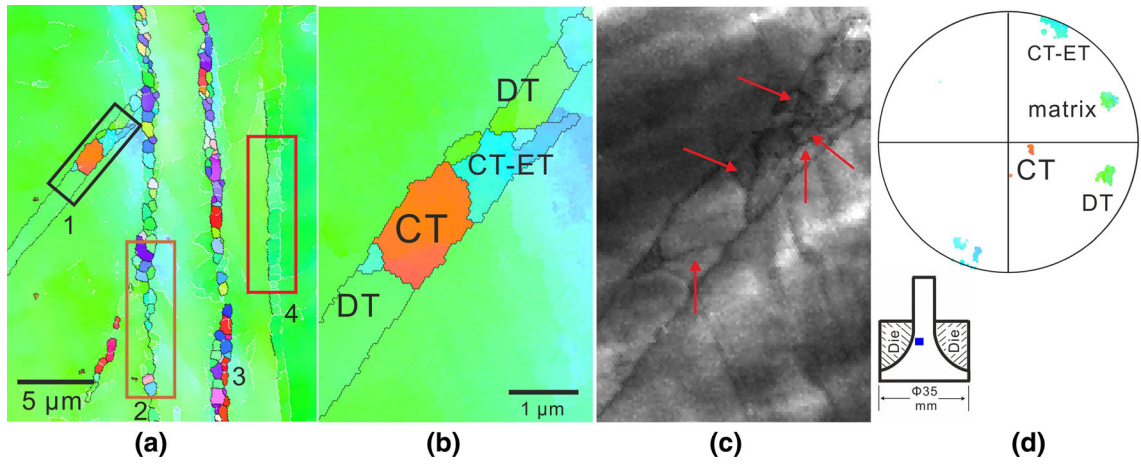


Fig. 8—(a) TKD orientation map of a partially recrystallized Mg-3Al-1Zn-1Ca-0.3Mn alloy. (b) Magnified TKD, (c) image-quality map, and (d) (0001) pole figure showing matrix, twins and subgrains.

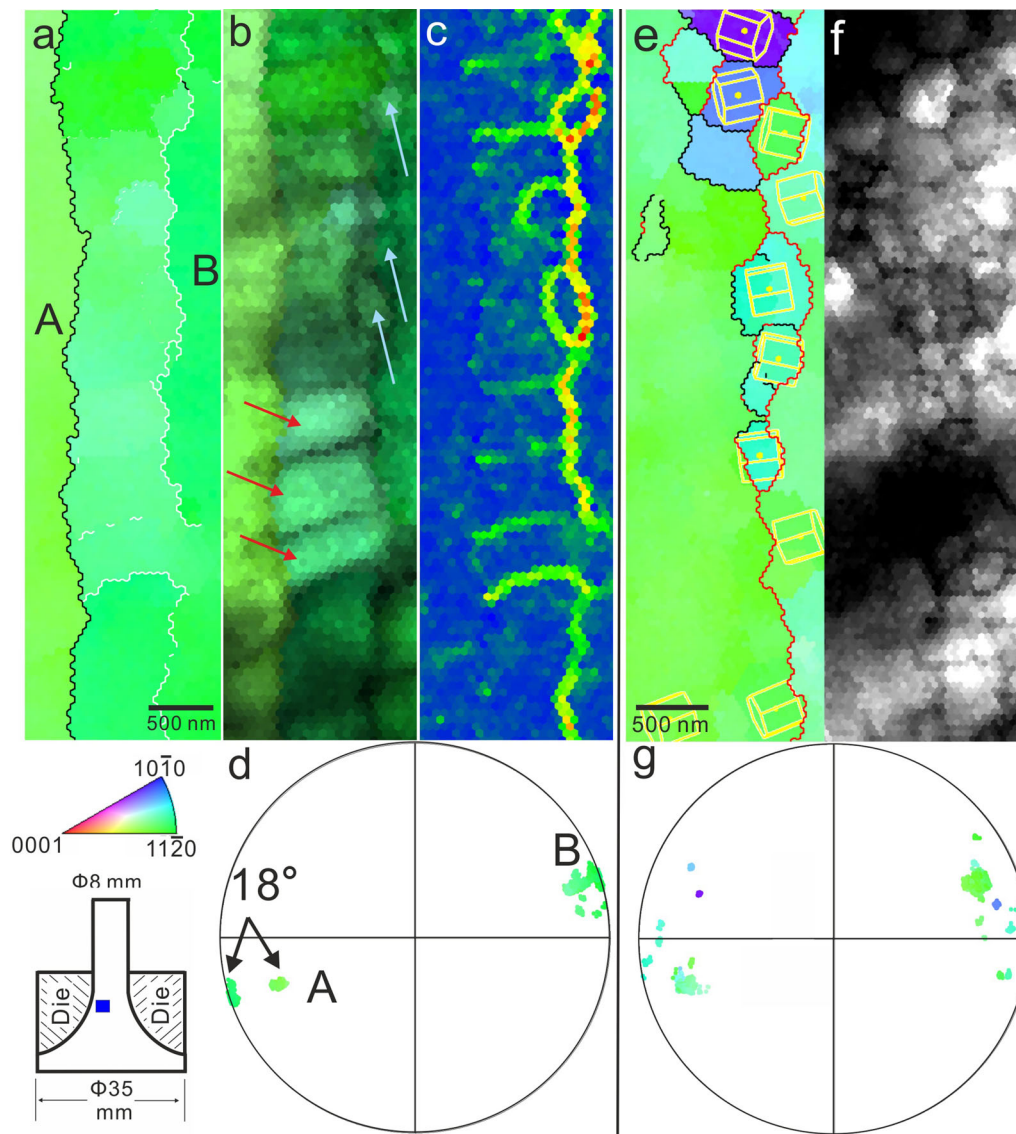


Fig. 9—Magnified illustration of grains and subgrains highlighted by (a through d) red and (d through g) orange rectangles in Fig. 8a in (a, e) orientation map, (b, f) image-quality map, and (c) KAM map, and (d, g) (0002) pole figure. Dark line in orientation map indicating HAGBs.



extrusion direction. These subgrains were identified as an early-stage state of first-generation recrystallized grains. On the LAGB of first-generation subgrains, several cellular subgrains highlighted by light-blue arrows were formed. The size of these second-generation cellular subgrains was even smaller, only about 100 to 150 nm in diameter. The KAM map showed the high stored energy of the LAGBs compared to the matrix (Figure 9(c)).<sup>[44]</sup> The first and second generations of recrystallized subgrains in the microband 4 had similar orientations (Figure 9(d)). As an example of later stage of DRX, the recrystallized grains in the microband 2 (Figures 9(e) through (g)) had larger misorientations (up to ~ 30 deg). On the boundary of recrystallized grains, more cellular subgrains were observed microband 4 (Figure 9(e)), which had an ultrafine grain size of about ~ 100 nm in diameter. Therefore, the DRX initiated from the microbands and progressed continuously in the Mg-3Al-1Zn-1Ca-0.3Mn alloy.

The DRX in microbands was widely observed in the Mg-3Al-1Zn-1Ca-0.3Mn alloy. The grain shown in Figure 10 had a different orientation to the grain in Figure 9, but the similar DRX behavior originating from microband was also observed. Within the grain shown in Figure 10(a), a pair of boundaries were also observed nearly parallel with the extrusion direction. The averaged grain boundary misorientations were about 20 deg (red arrow) and 10 deg (white arrow). These two boundaries formed a microband, with the interboundary space ranging from 500 to 800 nm. In the microband, there were dense LAGBs and numerous cellular subgrains (highlighted by red arrows in Figure 10(b)). These cellular subgrains had similar orientations to its parent grain. The superimposition of orientation map and KAM map (Figure 10(c)) shows that the LAGBs had much higher KAM value, indicating higher misorientation and stored energy.<sup>[39]</sup> The measurement showed a high accumulated misorientation (> 30 deg) along with white dashed line that crossed the band.

In some local areas of the partially recrystallized Mg-3Al-1Zn-1Ca-0.3Mn alloy, recrystallized grains were the major fraction (Figure 11). Under this circumstance, the residual deformed grains were highly elongated and had high in-grain misorientation. The LAGBs formed a network, which subdivided the residual deformed grains into numerous subgrains with different orientations, which were demonstrated by different colors of subgrains (Figures 11(a) and (b)). Along the dark, dashed line across the deformed grain, the orientation gradient was large, up to 30 deg (Figures 11(a) and (c)). It is expected that the recrystallized grains, which originated from these subgrains, would have randomized grain orientations, leading to texture weakening of the whole sample after full recrystallization.

### 3. Grain boundary segregation in extruded Mg-Al-Zn-Ca-Mn alloys

Grain boundaries of the extruded Mg-Al-Zn-Ca-Mn alloys were further examined using the EDS-STEM technique (Figure 12). Second-phase particles were

absent in most grain boundaries. Instead, solute segregation to grain boundaries was commonly observed. In the Mg-3Al-1Zn-1Ca-0.3Mn alloy, Al, Zn, and Ca were cosegregated to the grain boundary. When the Ca concentration was decreased from 1 to 0.5 wt pct, the cosegregation of Al, Zn, and Ca to grain boundary still occurred, but the segregation of Ca to grain boundary became less significant. In the Mg-3Al-1Ca-0.3Mn alloy, cosegregation of Al and Ca to grain boundary was clearly observed. In the Ca-containing alloys, Mn atoms did not segregate to grain boundaries, but form Al-Mn particles.

In addition to the HAGBs, the solute segregation was also observed in LAGBs. For example, the boundary shown in Figure 13 was composed of an array of edge dislocations, leading to a misorientation of 10 deg. The distance of dislocation cores in the low-angle grain boundary was about ~1.8 nm. The high contrast in the HAADF-STEM image at the dislocation cores indicated the solute segregation to the dislocation cores.

## IV. DISCUSSION

### A. Identification of Ca-Induced Strengthening Factors

In the present study, the experimental results show that the Ca addition to AZ31 benchmark leads to a significant strength increment, which is due to the combined effect of strengthening induced by solutes, dislocations, particles, and grain boundaries. Texture also affects the alloy strength,<sup>[45-48]</sup> but it is not commonly regarded as an independent strengthening mechanism. A stronger basal texture leads to higher strength predominantly by enhancing the effectiveness of other strengthening mechanisms such as dislocation strengthening and boundary strengthening. In this section, the major contributors to the strength of alloys in this study will be identified.

The contribution of dislocations to strengthening (denoted  $\sigma_d$ ) can be estimated using the following equation.

$$\sigma_d = \alpha M G b \sqrt{\rho}, \quad [2]$$

where  $\alpha$  is a constant (= 0.2),  $G$  is the shear modulus of Mg (17 GPa),  $b$  is the Burgers vector of the gliding dislocations for Mg ( $b = 0.32$  nm),  $M$  is the Taylor factor for tensile deformation along the extrusion direction, and  $\rho$  is the dislocation density measured by XRD. The dislocation density can also be indicated by the TKD results, in which the distribution of geometric necessary dislocation (GND) is calculated using TSL OIM software. The Burgers vector input is 0.32 nm for Mg and the maximum in-grain misorientation cutoff is 15 deg. The distribution of GND is shown in Figure 14. It is shown that, qualitatively, AZ31 has the lowest GND density ( $1.27 \times 10^{14}/\text{m}^2$ ) while the Mg-3Al-1Zn-1Ca-0.3Mn has the highest GND ( $4.36 \times 10^{14}/\text{m}^2$ ), which is consistent to the XRD result. Moreover, the density of GND estimated using EBSD is in the same order as the density of dislocation measured by XRD. However, the



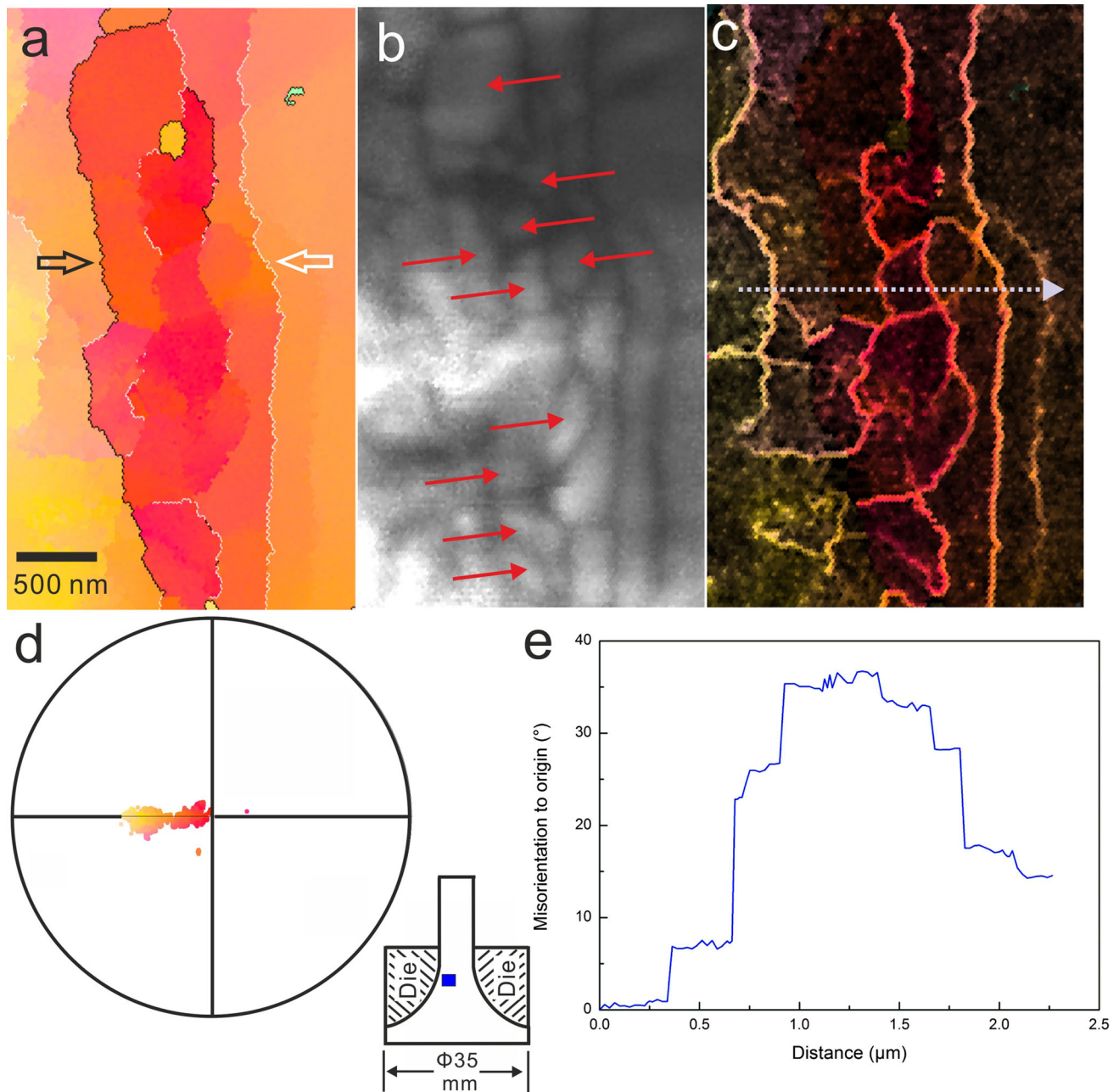


Fig. 10—(a) TKD orientation map, (b) image-quality map, (c) orientation-KAM map, and (d) (0002) pole figure of a deformed Mg-3Al-1Zn-1Ca-0.3Mn alloy, viewed along nearly [0001] axis. (e) Histogram showing the misorientation-to-origin along line profile in (c). Grain boundaries in dark indicating HAGBs.

dislocation density measured by XRD is more convincing, as XRD measurement counts both GND and statistically stored dislocation (SSD), which both contribute to dislocation strengthening.

Taylor factor ( $M$ ) for each alloy is calculated from their textures, using OIM TSL software. The input parameters for the calculation of  $M$ -value also include the critical resolved shear stresses, which are 50 MPa for basal slip and 100 MPa for prismatic slip.<sup>[49]</sup> The dislocation density and Taylor factor values for each alloy are listed in Table II. Using Eq. [2], the dislocation strengthening in AZ31 is estimated as  $\sim 42$  MPa. The Ca

addition increases the dislocation strengthening increment to the range 93 to 99 MPa.

With respect to grain boundary strengthening, both HAGBs and LAGBs can strengthen alloys. In a partially recrystallized sample, the strengthening increment induced by HAGBs (denoted  $\sigma_{\text{HAGB}}$ ) can be expressed by the modified Hall-Petch equation:<sup>[50]</sup>

$$\sigma_{\text{HAGB}} = k / \sqrt{D/f}, \quad [3]$$

where  $k$  is a constant of  $190 \text{ MPa } \mu\text{m}^{1/2}$  for the extruded AZ31 alloy, based on the previous experiments in the

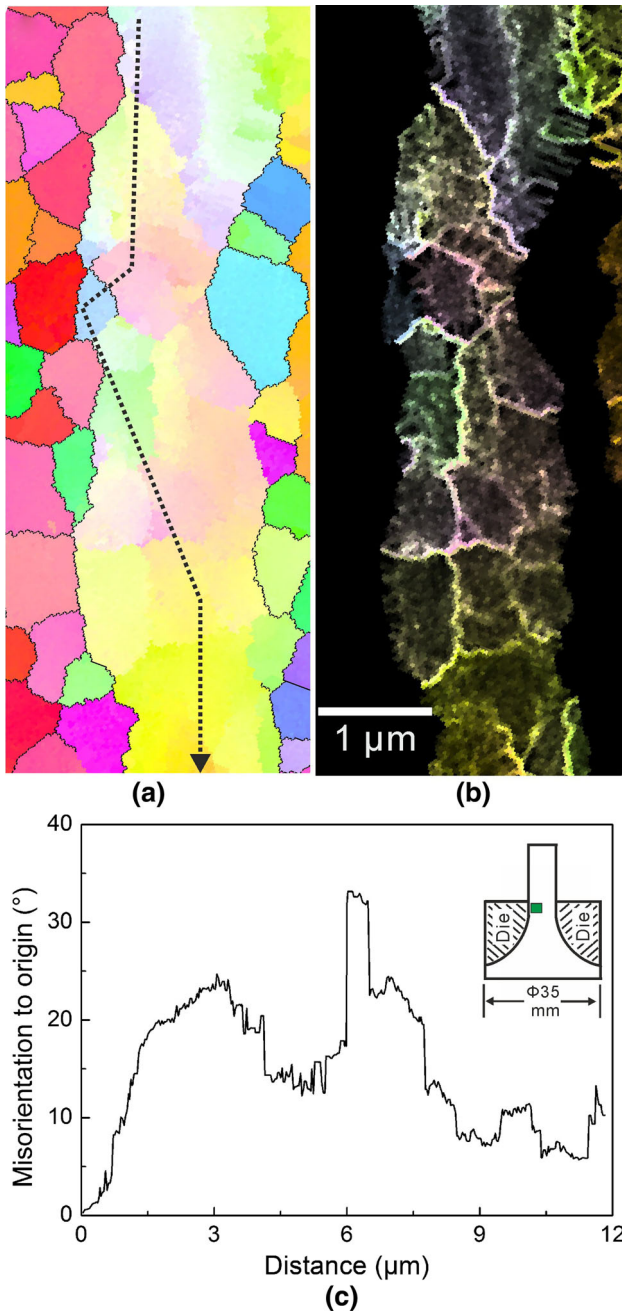


Fig. 11—(a) TKD-orientation map and (b) orientation-KAM map of a deformed Mg-3Al-1Zn-1Ca-0.3Mn alloy in the partially recrystallized region. (c) Histogram showing the misorientation-to-origin along line profile in (a).

same condition;<sup>[7]</sup> and  $f$  is the fraction of HAGBs among grain boundaries, which is 69 pct for the benchmark AZ31.  $D$  is the averaged grain size including subgrains, which is 2.3  $\mu\text{m}$  for the AZ31 (Table II). Using Eq. [3], the contribution of HAGBs to the strength of the benchmark AZ31 is calculated to be of 104 MPa.

The  $k$ -values for the Ca-containing alloys were also calculated. By fitting the yield strength and density of HAGBs ( $\frac{1}{\sqrt{D}f}$ ) of the samples extruded at 250 °C and 300 °C, the  $k$ -values were calculated to be about 194

MPa  $\mu\text{m}^{1/2}$  for Mg-3Al-1.5Zn-0.5Ca-0.3Mn, 212 MPa  $\mu\text{m}^{1/2}$  for Mg-3Al-1Zn-1Ca-0.3Mn alloy, and 245 MPa  $\mu\text{m}^{1/2}$  for Mg-3Al-1Ca-0.3Mn. Compared with the AZ31 benchmark, the Ca-containing alloys have higher  $k$ -values, which is likely to be caused by stronger alloy texture.<sup>[45–48]</sup> Based on Eq. [3], the strengthening increment induced by HAGBs was calculated to be  $\sim 108$  MPa in the Mg-3Al-1Zn-1Ca-0.3Mn and 105 MPa in the Mg-3Al-1Ca-0.3Mn, which are similar to that of the benchmark AZ31. For the Mg-3Al-1.5Zn-0.5Ca-0.3Mn alloy, the HAGB-induced strengthening is lower, about 84 MPa. Therefore, the HAGB-induced strengthening is not the key factor for the higher strength of the Mg-Al-Zn-Ca-Mn alloys than that of AZ31.

The contribution of LAGB ( $\sigma_{\text{LAGB}}$ ) can be expressed by the following equation:<sup>[50]</sup>

$$\sigma_{\text{LAGB}} = \alpha \text{MG} \sqrt{\frac{3b\theta_{\text{LAGB}}(1-f)}{D}}, \quad [4]$$

where  $\theta_{\text{LAGB}}$  is the misorientation angle (in radian) of the LAGBs. Using Eq. [4], the LAGB-induced strengthening in the AZ31 alloy is found to be only about 22 MPa. With the dilute addition of Ca, the LAGB-induced strengthening increment increases significantly to 63, 47, and 66 MPa for the Mg-3Al-1Zn-0.5Ca-0.3Mn, Mg-3Al-1Zn-1Ca-0.3Mn, and Mg-3Al-1Ca-0.3Mn alloys, respectively. The combined strengthening effects of dislocations and LAGBs can be analyzed using a pythagorean addition law ( $\sqrt{\sigma_{\text{d}}^2 + \sigma_{\text{LAGB}}^2}$ ).<sup>[51,52]</sup> By further comparing the measured yield strength (denoted  $\sigma_{\text{measured}}$ ) and the calculated  $\sigma_{\text{dislocation}}$ ,  $\sigma_{\text{LAGB}}$ , and  $\sigma_{\text{HAGB}}$  of the alloys, the higher densities of dislocations and LAGBs are found to be the key factor for the higher strength of the Ca-containing alloys, with respect to the AZ31 benchmark. For example, the Mg-3Al-1Zn-1Ca-0.3Mn has 96 MPa higher yield strength ( $\Delta\sigma_{\text{measured}}$ ) than the AZ31 alloy, when they are extruded at 250 °C. Among the 96 MPa strength increment, higher densities of dislocations and LAGBs,  $\Delta\sqrt{\sigma_{\text{d}}^2 + \sigma_{\text{LAGB}}^2}$ , are estimated to contribute  $\sim 68$  MPa increment, while HAGB ( $\sigma_{\text{HAGB}}$ ) only contributes  $\sim 4$  MPa increment. A gap of strength between  $\Delta\sigma_{\text{measured}}$  and sum of  $\Delta\sigma_{\text{HAGB}}$  and  $\Delta\sqrt{\sigma_{\text{d}}^2 + \sigma_{\text{LAGB}}^2}$  is noted. This gap,  $\sim 20$  to 25 MPa, is speculated to be caused by other strengthening factors, including solute and particle strengthening.

Al-Ca and Al-Mn particles are observed in the Mg-3Al-1Zn-1Ca-0.3Mn alloy using SEM and STEM (Figure 15). In SEM image, the particles have large size, and thus are likely to be the eutectic compound fragmented during extrusion. The interparticle space is estimated to be more than 20  $\mu\text{m}$ , and the particle size is observed in micron scale. Few Al-Ca and Al-Mn fine particles can also be observed in STEM image, but their density is too low to result in significant strengthening effect *via* Orowan effect. Hence, the strengthening increment induced by particles is deduced to be a minor factor, compared to the strengthening induced by boundaries and dislocations. This speculation is



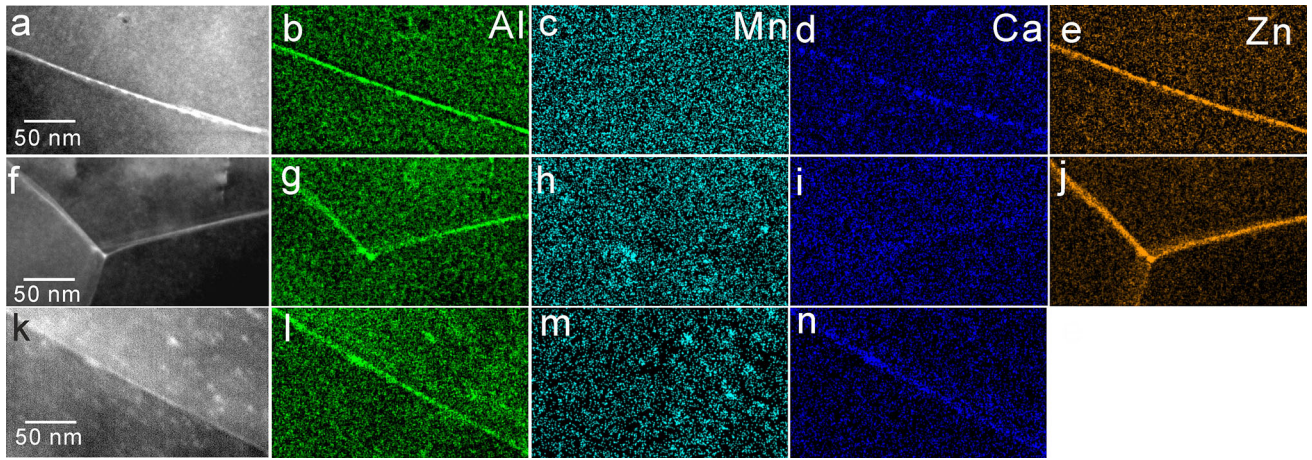


Fig. 12—HAADF-STEM and STEM-EDX mapping of (a through e) Mg-3Al-1Zn-1Ca-0.3Mn, (f through j) Mg-3Al-1.5Zn-0.5Ca-0.3Mn, and (k through n) Mg-3Al-1Ca-0.3Mn alloys extruded at 250 °C.

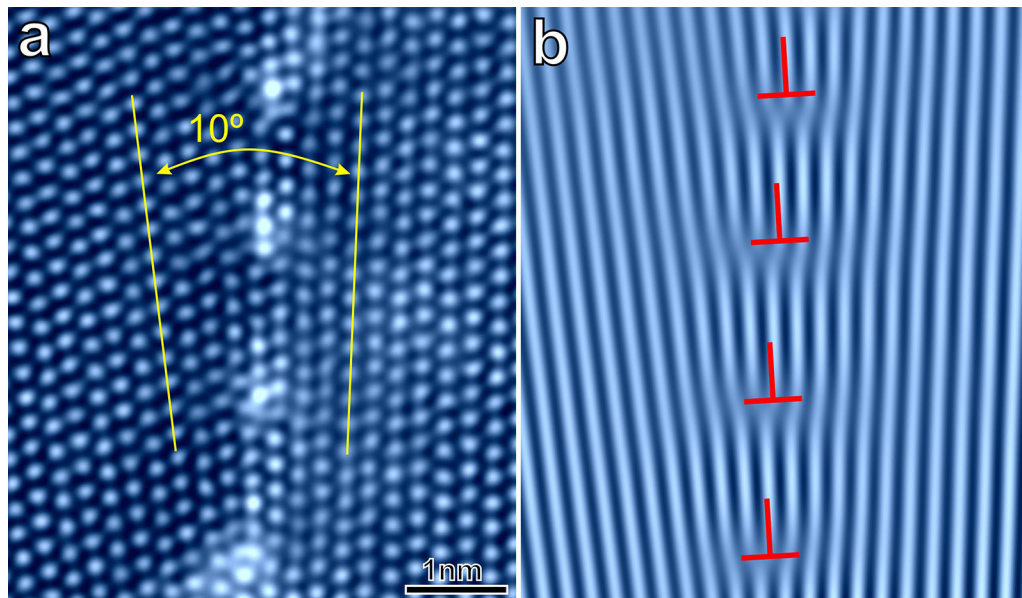


Fig. 13—HAADF-STEM images showing (a) cellular subgrains, and (b) low-angle grain boundaries. Image is viewed along  $[11\bar{2}0]$  direction.

consistent with previous studies in Mg-Ca-based alloys.<sup>[18,53]</sup> Hence, it is more important to understand how the Ca addition results in a different DRX behavior, which gives rise to much denser dislocations and LAGBs.

### B. Effect of Ca Addition on DRX During Extrusion

There are three main DRX mechanisms operative in magnesium and its alloys, namely continuous DRX (*c*DRX),<sup>[54–58]</sup> discontinuous DRX (*d*DRX),<sup>[18,59,60]</sup> and twin-induced DRX (*t*DRX).<sup>[43]</sup> In this study, the continuous DRX (*c*DRX), and twin-induced DRX (*t*DRX) are observed in the benchmark AZ31 (Figures 16(a) through (e)). During extrusion, the mobile dislocations

encounter barriers such as initial grain boundaries and form dislocation pile-up (Figure 16(b)). The dislocation pile-ups finally form subgrains enclosed by 3-dimensional LAGBs. The LAGBs continuously trap the dislocations that migrate toward the initial grain boundaries. At the same time, driven by the mechanical deformation, the subgrains will rotate.<sup>[61,62]</sup> Both dislocation collection and subgrain rotation will gradually transit subgrains to recrystallized grains, forming a ‘necklace’ microstructure (Figure 16(c)). This DRX mechanism is known as *c*DRX. It is also regarded as a strong dynamic recovery as there is no recognizable division between nucleation and grain growth stage.<sup>[62]</sup> With the progress of the extrusion process, the dislocations will accumulate at the boundaries of



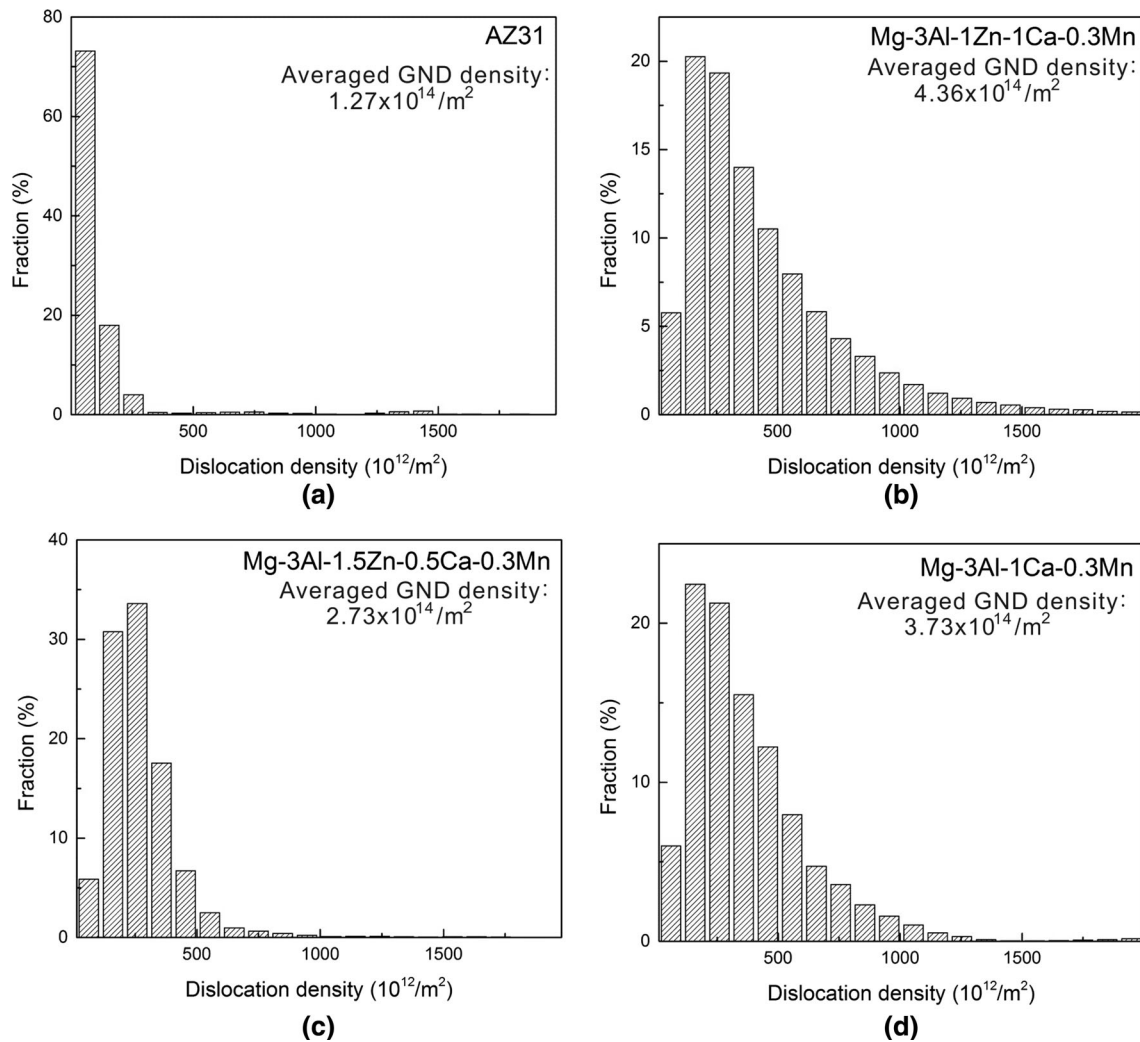


Fig. 14—Histograms showing distribution of geometric necessary dislocation in (a) AZ31, (b) Mg-3Al-1Zn-1Ca-0.3Mn, (c) Mg-3Al-1.5Zn-0.5Ca-0.3Mn, and (d) Mg-3Al-1Ca-0.3Mn alloys extruded at 250 °C.

first-generation DRXed grains (Figure 16(d)). Again, these accumulated dislocations form dislocation arrays, then subgrains and second-generation DRXed grains (Figure 16(e)).

Twin-induced DRX was also observed in the AZ31.<sup>[63,64]</sup> However, more recrystallized grains are observed outside of the deformation twin, where twin boundaries provide the sites for the dislocation pile-ups to form subgrains. Under this circumstance, there is no great difference between the roles of conventional HAGBs and former twin boundaries in *c*DRX.<sup>[63,65]</sup> The experimental observation suggests that the *c*DRX is the dominant DRX mechanism in the AZ31 alloy during extrusion.

Compared with the benchmark AZ31, the addition of Ca to AZ31 has two notable effects on microstructure, which eventually leads to the different behavior of *c*DRX during extrusion. The first microstructural change is cooperation of dislocation slip of different types, which is speculated to result in denser subgrains after extrusion. To support this speculation, we revisited

the TKD orientation maps of deformed grains and twins that contain subgrains in Figures 5, 6, 7, 8, 9, 10, and 11, and examined the distribution of Taylor axis (Figure 17). The AZ31 alloy was found to have a [0001]-type distribution of in-grain misorientation axis, *i.e.*, a misorientation axis distribution that was mostly concentrated near [0001] with the intensity of above 2  $\mu\text{d}$ . This indicates that during extrusion of AZ31 at 250 °C, prismatic  $\langle a \rangle$  dislocation is dominant in the region where subgrains form. Under the same extrusion condition, the Mg-3Al-1Zn-1Ca-0.3Mn alloy exhibits a uniform distribution of in-grain misorientation axis. Although the morphology and orientation of deformed grains and twins that contain subgrains in Figures 7, 8, 9, 10, and 11 are different from each other, the intensity of in-grain misorientation axis distribution is mostly between 1 and 1.5  $\mu\text{d}$ . The uniform distribution of in-grain misorientation axis indicates that there is no dominant slip mode, and dislocation slips in different systems are cooperating. In order to form subgrains during *c*DRX, mutual reaction of dislocations of

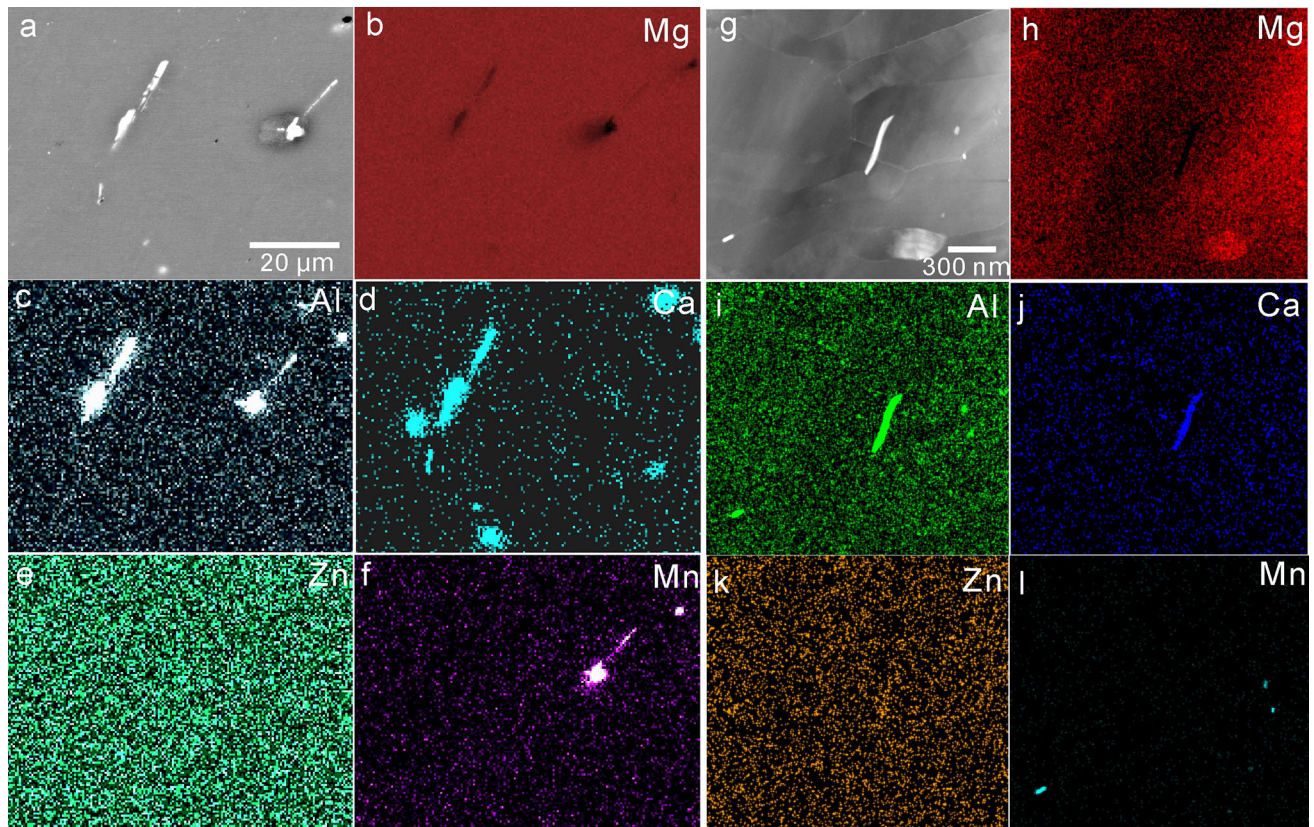


Fig. 15—(a) SEM backscattered electron image, (b through f) SEM-EDX maps, (g) HAADF-STEM and (h through l) STEM-EDX maps showing particles in Mg-3Al-1Zn-1Ca-0.3Mn alloy extruded at 250 °C.

different Burgers vectors are required to form three-dimensional arrays of LAGBs.<sup>[43]</sup> Therefore, compared with the DRX in AZ31, higher dislocation density (revealed by XRD in Figure 3) and significant cooperation of dislocation slip of different types is speculated to facilitate the formation of denser subgrains in Mg-3Al-1Zn-1Ca-0.3Mn alloy.

The second microstructural change caused by the Ca addition is the segregation of Ca to HAGBs (Figure 12) and possibly dislocation core in LAGBs, which may lead to a sluggish *c*DRX. Although there is a large amount of subgrains, they are difficult to transform into recrystallized grains. The solute-induced retardation of recrystallization in Mg alloys has been reported by several studies.<sup>[20,37,66,67]</sup> In this study, cosegregation of Al, Zn, and Ca atoms to boundaries have been observed in Ca-containing alloys. In this study, cosegregation of Al, Zn, and Ca atoms to boundaries has been observed in Ca-containing alloys. The Ca addition may change the amount of Al solute segregated to grain boundaries, as Ca atoms will form eutectic compound with Al during casting. However, such change in Al segregation would lead to minor effect on DRX behavior, given that segregation of Al atoms also occurs in benchmark AZ31, but AZ31 recrystallized readily. Hence, we suppose that Al segregation to grain boundary would not be an important factor for DRX retardation. Furthermore,

Zn segregation to grain boundaries is unlikely to be an important factor either, because DRX is still retarded in Mg-3Al-1Ca-0.3Mn alloy even though Zn is absent. However, once the Ca concentration is decreased, *e.g.*, from 1 to 0.5 wt pct, the DRX is notably more operative (Table II). Therefore, it is Ca segregation, rather than Al and Zn segregation to grain boundary that plays a significant role on the retardation of DRX. The atomic radius is 0.197 nm for Ca and 0.160 nm for Mg. Similar to the role of rare-earth elements on DRX in Mg,<sup>[68]</sup> substitution of Mg by Ca leads to a positive misfit of 0.231. Once Ca atoms segregate to the extension region of the dislocation cores in grain boundary, the elastic strain of grain boundary is reduced, making grain boundary less mobile. Consequently, the conversion from dislocations/LAGB to HAGB takes longer time and growth of recrystallized grain is retarded, as schematically illustrated in Figures 16(f) through (i).

In previous studies, the Ca effect on DRX in Ca-containing alloys was predominantly interpreted by the particle effect.<sup>[17,69,70]</sup> Ca has a maximum solubility of 1 wt pct in Mg at the eutectic temperature of 510 °C. The addition of Ca to the AZ-series alloy may lead to the formation of several types of eutectic intermetallics during casting, including (Mg,Al)<sub>2</sub>Ca and Mg<sub>2</sub>Ca or Al<sub>2</sub>Ca.<sup>[71]</sup> Upon hot working, the eutectic compounds are fragmented and distributed along the extrusion



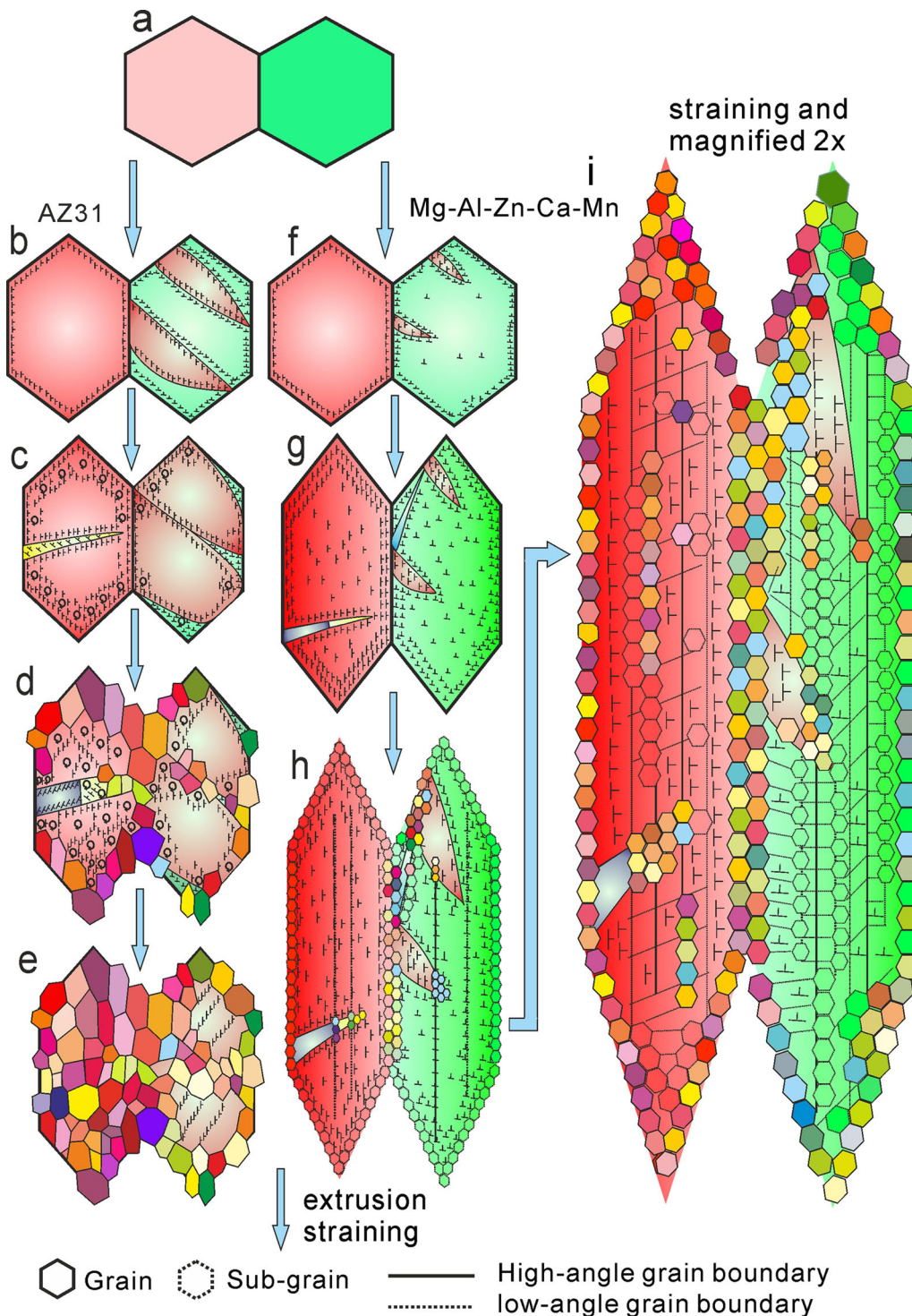


Fig. 16—Schematic diagram of (a) bi-grain microstructure showing dynamic recrystallization process in (b through e) AZ31 and (f through i) Mg-3Al-1Zn-1Ca-0.3Mn alloy subjected to the increasing strain during extrusion process. (i) is magnified by 2 times to show the detailed microstructural features.

direction. The fragments interact with grain boundaries, and suppress DRX and grain growth [17]. However, SEM and STEM images (Figure 15) reveal that the density of Al-Ca particles in the Mg-3Al-1Zn-1Ca-0.3Mn alloy is low, and that sparsely placed particles

are unlikely to restrict the size of subgrains and recrystallized grains in the submicron scale. With respect to Al-Mn particles, their effects on the retardation of DRX are likely limited, because the AZ31 alloy contains a high density of Al-Mn particle, but DRX can readily



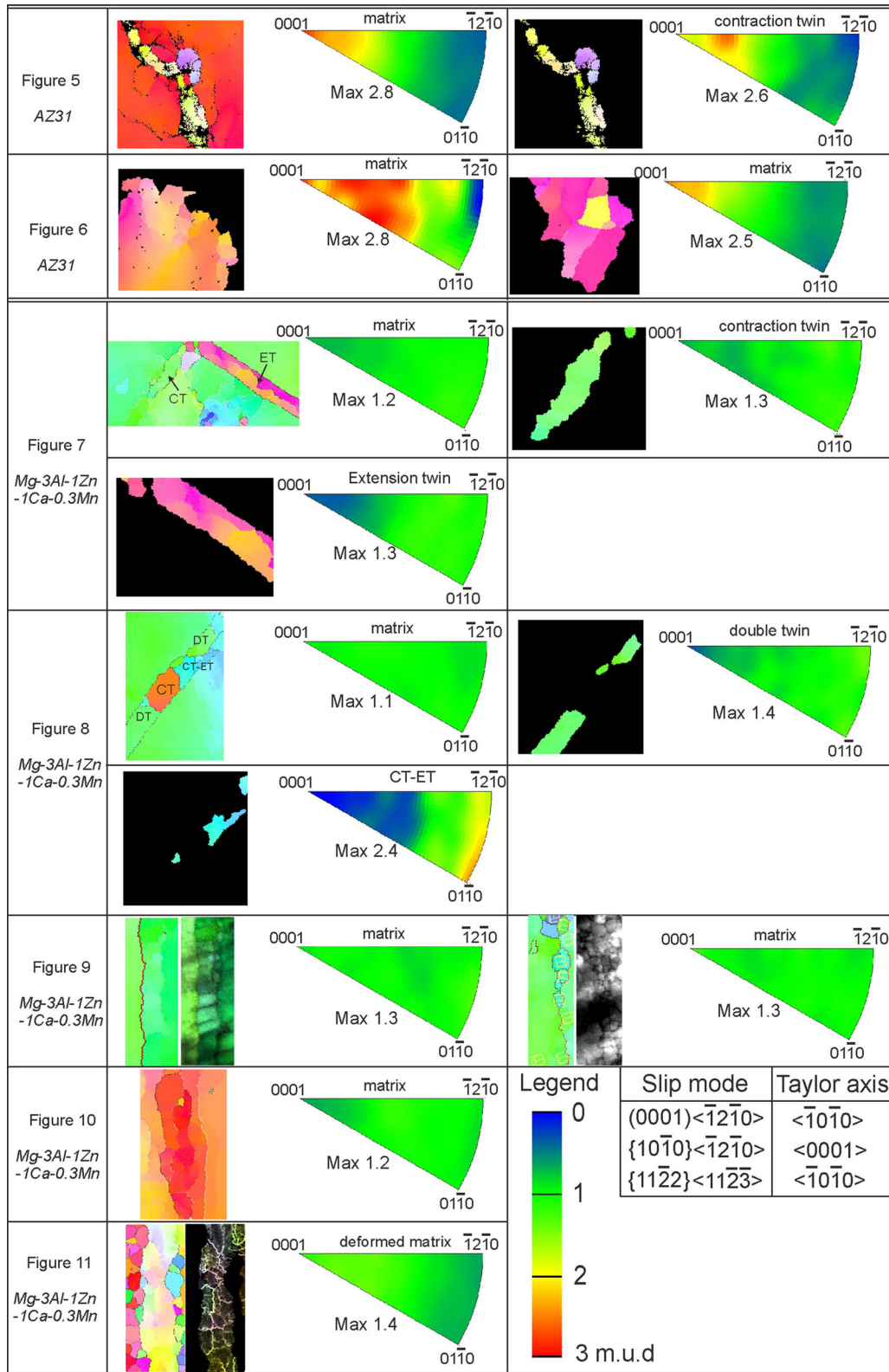


Fig. 17—IGMA analysis of deformed grains and twins that contain subgrains (displayed in Figures 5, 6, 7, 8, and 11) in AZ31 and Mg-3Al-1Zn-1Ca-0.3Mn alloys extruded at 250 °C.

operate.<sup>[7,72]</sup> Furthermore, the characterization of several regions where the sluggish *c*DRX occurs in the Mg-Al-Zn-Ca-Mn alloys (Figures 7, 8, 9, 10 and 11)

does not show the presence of the particles there. Therefore, particles are not likely to be the major factor for the retarded DRX.

## V. CONCLUSIONS

- a. Extruded Mg-Al-Zn-Ca-Mn-based alloys exhibit high strength at room temperature. The yield strength of Mg-3Al-1Zn-1Ca-0.3Mn extruded at 250 °C is as high as 413 MPa, with an elongation to fracture of 7.5 pct. The addition of Ca was key to achieving such high strength. The addition of 1 wt pct Ca to the benchmark AZ31 alloy led to a strengthening effect of ~96 MPa. In contrast, the addition of 1 wt pct Zn to Mg-3Al-1Ca-0.3Mn alloy only leads to a marginal increment in strength.
- b. The as-extruded AZ31 benchmark was near fully recrystallized. During extrusion, DRX progresses continuously, predominantly *via* the ready formation of subgrains (about 0.4 to 1  $\mu\text{m}$ ) along initial grain boundaries. The subgrains grow and convert to recrystallized grains with an average size of ~ 2.3  $\mu\text{m}$ .
- c. Calcium additions to the AZ31 benchmark retard dynamic recrystallization (DRX), with only 30 pct recrystallization and a grain size of 480 nm achieved following extrusion at 250 °C with a ram speed of 0.1 mm/s. A high density of low-angle grain boundaries (LAGBs) and dislocations were observed in the Ca-containing alloys, and it was identified as the major strengthening factor.
- d. In the case of the Mg-3Al-1Zn-1Ca-0.3Mn alloy, the cellular subgrains possess an ultrafine size of 100 to 400 nm and are sluggish to grow and convert to recrystallized grains during extrusion. Such subgrains are predominantly along initial grain boundaries and the newly formed boundaries within the deformed grains. These newly formed boundaries are closely spaced (*e.g.*, ~ 600 nm) and nearly parallel to the extrusion direction, forming microbands. The DRX in microbands was rarely observed in the AZ31.
- e. Solute atoms, including Al, Zn, and Ca, were observed to segregate to HAGBs and to dislocation cores in LAGBs. It is hypothesized that the segregation of Ca to dislocation cores will decrease the mobility of dislocations and stabilize low-angle grain boundaries, *via* thermodynamically decreasing dislocation energy and/or kinetically solute drag effect. In this way, the Ca addition retards the DRX and grain growth in the Ca-containing alloys during the extrusion process, leaving a high density of boundaries and dislocations, which result in the high strength.

## ACKNOWLEDGMENTS

The authors are grateful for the financial support from the Australian Research Council and Baoshan Iron & Steel Co., Ltd. We acknowledge the permission for the use of facilities at the Monash Center for Electron Microscopy. Special thanks to Enrico Seemann

for the help with extrusion, and Lingyu Wang and Wuxiang Wu for helpful discussion in the XRD analysis.

## REFERENCES

1. T.M. Pollock: *Science*, 2010, vol. 328, pp. 986–87.
2. W.J. Joost and P.E. Krajewski: *Scr. Mater.*, 2017, vol. 128, pp. 107–12.
3. M. Liu, Y. Guo, J. Wang, and M. Yergin: *npj Mater. Degrad.*, 2018, vol. 2, p. 24.
4. I.J. Polmear, D. StJohn, J.F. Nie, and M. Qian: *Light Alloys*, 5th ed., Butterworth-Heinemann, Boston, 2017.
5. Z.R. Zeng, N. Stanford, C.H.J. Davies, J.F. Nie, and N. Birbilis: *Int. Mater. Rev.*, 2018, pp. 1–36.
6. T.B. Abbott: *Corrosion*, 2015, vol. 71, pp. 120–27.
7. Z.R. Zeng, Y.M. Zhu, R.L. Liu, S.W. Xu, C.H.J. Davies, J.F. Nie, and N. Birbilis: *Acta Mater.*, 2018, vol. 160, pp. 97–108.
8. Y. Kawamura, K. Hayashi, A. Inoue, and T. Masumoto: *Mater. Trans.*, 2001, vol. 42, pp. 1171–74.
9. T. Homma, N. Kunito, and S. Kamado: *Scr. Mater.*, 2009, vol. 61, pp. 644–47.
10. C. Xu, M.Y. Zheng, S.W. Xu, K. Wu, E.D. Wang, G.H. Fan, and S. Kamado: *Mater. Sci. Eng. A*, 2015, vol. 643, pp. 137–41.
11. Z.J. Yu, Y.D. Huang, X. Qiu, G.F. Wang, F.Z. Meng, N. Hort, and J. Meng: *Mater. Sci. Eng. A*, 2015, vol. 622, pp. 121–30.
12. C. Xu, M.Y. Zheng, S.W. Xu, K. Wu, E.D. Wang, S. Kamado, G.J. Wang, and X.Y. Lv: *Mater. Sci. Eng. A*, 2012, vol. 547, pp. 93–98.
13. J.F. Nie: *Metall. Mater. Trans. A*, 2012, vol. 43, pp. 3891–939.
14. T.T. Sasaki, K. Yamamoto, T. Honma, S. Kamado, and K. Hono: *Scr. Mater.*, 2008, vol. 59, pp. 1111–14.
15. T.T. Sasaki, F.R. Elsayed, T. Nakata, T. Ohkubo, S. Kamado, and K. Hono: *Acta Mater.*, 2015, vol. 99, pp. 176–86.
16. S.H. Park, J.G. Jung, Y.M. Kim, and B.S. You: *Mater. Lett.*, 2015, vol. 139, pp. 35–38.
17. S.W. Xu, K. Oh-ishi, S. Kamado, F. Uchida, T. Homma, and K. Hono: *Scr. Mater.*, 2011, vol. 65, pp. 269–72.
18. H.C. Pan, G.W. Qin, Y.M. Huang, Y.P. Ren, X.C. Sha, X.D. Han, Z.Q. Liu, C.F. Li, X.L. Wu, H.W. Chen, C. He, L.J. Chai, Y.Z. Wang, and J.F. Nie: *Acta Mater.*, 2018, vol. 149, pp. 350–63.
19. A.A. Nayeb-Hashemi and J.B. Clark: *Phase Diagrams of Binary Magnesium Alloys*, ASM International, Materials Park, OH, 1985.
20. Z.R. Zeng, Y.M. Zhu, S.W. Xu, M.Z. Bian, C.H.J. Davies, N. Birbilis, and J.F. Nie: *Acta Mater.*, 2016, vol. 105, pp. 479–94.
21. N. Stanford and M. Barnett: *Mater. Sci. Eng. A*, 2008, vol. 496, pp. 399–408.
22. Y. Chino, T. Ueda, Y. Otomatsu, K. Sassa, X.S. Huang, K. Suzuki, and M. Mabuchi: *Mater. Trans.*, 2011, vol. 52, pp. 1477–82.
23. M.Z. Bian, T.T. Sasaki, B.C. Suh, T. Nakata, S. Kamado, and K. Hono: *Scr. Mater.*, 2017, vol. 138, pp. 151–55.
24. Y. Chino, K. Sassa, X.S. Huang, K. Suzuki, and M. Mabuchi: *J. Jpn. Inst. Met. Mater.*, 2011, vol. 75, pp. 35–41.
25. J.Y. Lee, Y.S. Yun, B.C. Suh, N.J. Kim, W.T. Kim, and D.H. Kim: *J. Alloy Compd.*, 2014, vol. 589, pp. 240–46.
26. M.Z. Bian, Z.R. Zeng, S.W. Xu, S.M. Zhu, Y.M. Zhu, C.H.J. Davies, N. Birbilis, and J.F. Nie: *Adv. Eng. Mater.*, 2016, vol. 18, pp. 1763–69.
27. B.P. Zhang, Y. Wang, L. Geng, and C.X. Lu: *Mater. Sci. Eng. A*, 2012, vol. 539, pp. 56–60.
28. V.M. Miller and T.M. Pollock: *Metall. Mater. Trans. A*, 2016, vol. 47A, pp. 1854–64.
29. Z.R. Zeng, M.Z. Bian, S.W. Xu, C.H.J. Davies, N. Birbilis, and J.F. Nie: *Mater. Sci. Eng. A*, 2016, vol. 674, pp. 459–71.
30. T. Nakata, C. Xu, R. Ajima, K. Shimizu, S. Hanaki, T.T. Sasaki, L. Ma, K. Hono, and S. Kamado: *Acta Mater.*, 2017, vol. 130, pp. 261–70.
31. T. Nakata, T. Mezaki, C. Xu, K. Oh-ishi, K. Shimizu, S. Hanaki, and S. Kamado: *J. Alloy Compd.*, 2015, vol. 648, pp. 428–37.
32. G.C. Sneddon, P.W. Trimby, and J.M. Cairney: *Mater. Sci. Eng. R*, 2016, vol. 110, pp. 1–12.



33. P.W. Trimby, Y. Cao, Z.B. Chen, S. Han, K.J. Hemker, J.S. Lian, X.Z. Liao, P. Rottmann, S. Samudrala, J.L. Sun, J.T. Wang, J. Wheeler, and J.M. Cairney: *Acta Mater.*, 2014, vol. 62, pp. 69–80.
34. K. Lu: *Nat. Rev. Mater.*, 2016, vol. 1, p. 16019.
35. M.F. Ashby: *Philos. Mag.*, 1970, vol. 21, pp. 399–424.
36. Y.B. Chun and C.H.J. Davies: *Metall. Mater. Trans. A*, 2011, vol. 42A, pp. 4113–25.
37. J.P. Hadorn, K. Hantzsche, S.B. Yi, J. Bohlen, D. Letzig, J.A. Wollmershauser, and S.R. Agnew: *Metall. Mater. Trans. A*, 2016, vol. 47A, pp. 1854–64.
38. G.K. Williamson and R.E. Smallman: *Philos. Mag. A*, 1956, vol. 1, pp. 34–46.
39. D. Balzar and H. Ledbetter, *Advances in X-ray Analysis* 1995, vol. 38.
40. M. Wiessner, E. Gamsjäger, S.V.D. Zwaag, and P. Angerer: *Mater. Sci. Eng. A*, 2017, vol. 682, pp. 117–25.
41. I.C. Dragomir and T. Ungar: *J. Appl. Crystallogr.*, 2002, vol. 35, pp. 556–64.
42. S.I. Wright and M.M. Nowell: *Microsc. Microanal.*, 2006, vol. 12, pp. 72–84.
43. C. Bettles and M. Barnett: *Advances in Wrought Magnesium Alloys: Fundamentals of Processing, Properties and Applications*, Elsevier, Amsterdam, 2012.
44. S.I. Wright, M.M. Nowell, and D.P. Field: *Microsc. Microanal.*, 2011, vol. 17, pp. 316–29.
45. H.H. Yu, C.Z. Li, Y.C. Xin, A. Chapuis, X.X. Huang, and Q. Liu: *Acta Mater.*, 2017, vol. 128, pp. 313–26.
46. W. Yuan, S.K. Panigrahi, J.Q. Su, and R.S. Mishra: *Scr. Mater.*, 2011, vol. 65, pp. 994–97.
47. Y. Wang and H. Choo: *Acta Mater.*, 2014, vol. 81, pp. 83–97.
48. Y.N. Wang, C.I. Chang, C.J. Lee, H.K. Lin, and J.C. Huang: *Scr. Mater.*, 2006, vol. 55, pp. 637–40.
49. M.R. Barnett, Z. Keshavarz, and X. Ma: *Metall. Mater. Trans. A*, 2006, vol. 37A, pp. 2283–93.
50. N. Hansen: *Scr. Mater.*, 2004, vol. 51, pp. 801–06.
51. D. Kuhlmann-Wilsdorf: *Mater. Sci. Eng. A*, 1989, vol. 113, pp. 1–41.
52. T.L. Huang, L.F. Shuai, A. Wakeel, G.L. Wu, N. Hansen, and X.X. Huang: *Acta Mater.*, 2018, vol. 156, pp. 369–78.
53. F. Naghdi, R. Mahmudi, J.Y. Kang, and H.S. Kim: *Philos. Mag.*, 2015, vol. 95, pp. 3452–66.
54. S. Biswas, S.S. Dhinwal, and S. Suwas: *Acta Mater.*, 2010, vol. 58, pp. 3247–61.
55. A.G. Beer and M.R. Barnett: *Metall. Mater. Trans. A*, 2007, vol. 38A, pp. 1856–67.
56. J.C. Tan and M.J. Tan: *Mater. Sci. Eng. A*, 2003, vol. 339, pp. 124–32.
57. X.Y. Yang, Z.S. Ji, H. Miura, and T. Sakai: *Trans. Nonferr. Met. Soc.*, 2009, vol. 19, pp. 55–60.
58. A. Galiyev, R. Kaibyshev, and G. Gottstein: *Acta Mater.*, 2001, vol. 49, pp. 1199–207.
59. D.K. Sun, C.P. Chang, and P.W. Kao: *Metall. Mater. Trans. A*, 2010, vol. 41A, pp. 1864–70.
60. E. Martin and J.J. Jonas: *Acta Mater.*, 2010, vol. 58, pp. 4253–66.
61. R. Kaibyshev, K. Shipilova, F. Musin, and Y. Motohashi: *Mater. Sci. Eng. A*, 2005, vol. 396, pp. 341–51.
62. F.J. Humphreys and M. Hatherly: *Recrystallisation and Related Annealing Phenomena*, 2nd ed., Elsevier, Oxford, 2004.
63. K.D. Molodov, T. Al-Samman, D.A. Molodov, and G. Gottstein: *Acta Mater.*, 2014, vol. 76, pp. 314–30.
64. T. Al-Samman and G. Gottstein: *Mater. Sci. Eng. A*, 2008, vol. 490, pp. 411–20.
65. T. Al-Samman, K.D. Molodov, D.A. Molodov, G. Gottstein, and S. Suwas: *Acta Mater.*, 2012, vol. 60, pp. 537–45.
66. N. Stanford, G. Sha, J.H. Xia, S.P. Ringer, and M.R. Barnett: *Scr. Mater.*, 2011, vol. 65, pp. 919–21.
67. J.D. Robson: *Metall. Mater. Trans. A*, 2014, vol. 45A, pp. 3205–12.
68. D. Griffiths: *Mater. Sci. Technol.*, 2014, vol. 31, pp. 10–24.
69. S.W. Xu, S. Kamado, and T. Honma: *Scr. Mater.*, 2010, vol. 63, pp. 293–96.
70. G.T. Bae, J.H. Bae, D.H. Kang, H. Lee, and N.J. Kim: *Met. Mater. Int.*, 2009, vol. 15, pp. 1–5.
71. A. Suzuki, N.D. Saddock, J.W. Jones, and T.M. Pollock: *Acta Mater.*, 2005, vol. 53, pp. 2823–34.
72. N. Stanford and D. Atwell: *Metall. Mater. Trans. A*, 2013, vol. 44, pp. 4830–43.

**Publisher's Note** Springer Nature remains neutral with regard to jurisdictional claims in published maps and institutional affiliations.